Head-on collisions of binary white dwarf-neutron stars: Simulations in full general relativity

Vasileios Paschalidis,[1] Zachariah Etienne,[1] Yuk Tung Liu,[1] and Stuart L. Shapiro[1,2]

[1]*Department of Physics, University of Illinois at Urbana-Champaign, Urbana, Illinois 61801, USA*

[2]*Department of Astronomy and NCSA, University of Illinois at Urbana-Champaign, Urbana, Illinois 61801, USA*

(Received 21 September 2010; published 1 March 2011)

We simulate head-on collisions from rest at large separation of binary white dwarf-neutron stars (WDNSs) in full general relativity. Our study serves as a prelude to our analysis of the circular binary WDNS problem. We focus on compact binaries whose total mass exceeds the maximum mass that a cold-degenerate star can support, and our goal is to determine the fate of such systems. A fully general relativistic hydrodynamic computation of a realistic WDNS head-on collision is prohibitive due to the large range of dynamical time scales and length scales involved. For this reason, we construct an equation of state (EOS) which captures the main physical features of neutron stars (NSs) while, at the same time, scales down the size of white dwarfs (WDs). We call these scaled-down WD models "pseudo-WDs (pWDs)." Using pWDs, we can study these systems via a sequence of simulations where the size of the pWD gradually increases toward the realistic case. We perform two sets of simulations; One set studies the effects of the NS mass on the final outcome, when the pWD is kept fixed. The other set studies the effect of the pWD compaction on the final outcome, when the pWD mass and the NS are kept fixed. All simulations show that after the collision, 14%–18% of the initial total rest mass escapes to infinity. All remnant masses still exceed the maximum rest mass that our *cold* EOS can support ($1.92M_\odot$), but no case leads to prompt collapse to a black hole. This outcome arises because the final configurations are *hot*. All cases settle into spherical, quasiequilibrium configurations consisting of a cold NS core surrounded by a hot mantle, resembling Thorne-Zytkow objects. Extrapolating our results to realistic WD compactions, we predict that the likely outcome of a head-on collision of a realistic, massive WDNS system will be the formation of a quasiequilibrium Thorne-Zytkow-like object.

DOI: 10.1103/PhysRevD.83.064002 PACS numbers: 04.25.D−, 04.25.dk, 04.40.Dg

I. INTRODUCTION

The inspiral and merger of compact binaries represent some of the most promising sources of gravitational waves (GWs) for detection by ground-based laser interferometers like LIGO [1,2], VIRGO [3,4], GEO [5], TAMA [6,7] and AIGO [8], as well as by the proposed space-based interferometers LISA [9] and DECIGO [10]. Extracting physical information from gravitational radiation emitted by compact binaries and determining their ultimate fate requires careful modeling of these systems in full general relativity (see [11] and references therein). Most effort to date has focused on modeling black hole-black hole binaries (see [12] and references therein), and neutron star-neutron star binaries (see [13] for a review), with some recent general relativistic work on black hole-neutron star binaries [14–32].

In this work we consider white dwarf-neutron star (WDNS) binaries in full general relativity. WDNS binaries are promising sources of low-frequency GWs for LISA and DECIGO and, as we argued in [33], possibly also high-frequency GWs for LIGO, VIRGO, GEO, TAMA, and AIGO, if the remnant ultimately collapses to form a black hole.

Like neutron star-neutron star binaries, WDNS binaries are known to exist. In [33] we compiled tables with 20 observed WDNS binaries and their orbital properties. The neutron star (NS) masses in these systems range between $1.26M_\odot$ and $2.08M_\odot$, and their distribution is centered around $1.5M_\odot$. On the other hand, the WD masses in these systems range between $0.125M_\odot$ and $1.3M_\odot$, and their distribution is centered around $0.6M_\odot$. Finally, 18 of these observed WDNS binaries have total mass greater than $1.65M_\odot$, of which 8 have a WD component with mass greater than $0.8M_\odot$, and 5 have total mass greater than $2.2M_\odot$. This is interesting because the expected Tolman-Oppenheimer-Volkoff (TOV) limiting mass for a cold, degenerate gas ranges between $1.65M_\odot$ and $2.2M_\odot$ [34–42], depending on the equation of state (EOS) and degree of rotation, and one of the main goals of this work is to determine whether a WDNS merger can lead to prompt collapse to a black hole.

Population synthesis calculations by Nelemans *et al.* [43] show that there are about 2.2×10^6 WDNS binaries in our Galaxy, and that they have a merger rate of 1.4×10^{-4} yr^{-1}. Furthermore, Nelemans *et al.* find that after a year of integration, LISA should be able to detect 128 WDNS pre-merger binaries and, after considering the contribution of the double WD background GW noise, resolve 38 of these. On the other hand, calculations by Cooray [44] give much more conservative numbers of resolvable WDNS binaries. In particular, Cooray finds that the number of LISA-resolvable WDNS binaries ranges between 1–10, using a WDNS merger rate between 10^{-6} yr^{-1}–10^{-5} yr^{-1}. Finally, recent

work by Thompson *et al.* [45] suggests that the lower limit on the merger rate in the Milky Way, at 95% confidence, is 2.5×10^{-5} yr^{-1}. Thompson *et al.* also suggest that the merger rate in the local universe is $\sim 0.5\text{–}1 \times 10^4$ Gpc^{-3} yr^{-1}. Therefore, leaving some uncertainties aside, all recent work on population synthesis suggests that LISA should be able to detect a few WDNS premergers per year.

We note here that Newtonian work on binaries with a WD component has been performed analytically in [33,46–50] and via Newtonian hydrodynamic simulations in [51–56].

In [33] we focused on WDNS binaries that have spiraled sufficiently close that they reach the termination point for equilibrium configurations. This is the Roche limit for WDNSs, at which point the WD fills its Roche lobe and may experience one of at least two possible fates: (i) stable mass transfer (SMT) from the WD across the inner Lagrange point onto the NS, or (ii) tidal disruption of the WD by the NS via unstable mass transfer (UMT).

We also studied the key parameters that determine whether a system will undergo SMT or UMT and found that, for a given NS mass, there exists a critical mass ratio $q_{\rm crit} \approx 2/3$ which separates the UMT and SMT regimes. If the mass ratio $q = M_{\rm WD}/M_{\rm NS}$ of a WDNS system is such that $q > q_{\rm crit}$, the WD quickly overfills its Roche lobe, and the binary will ultimately undergo UMT. In the opposite case, $q < q_{\rm crit}$, the system will undergo SMT. We showed that a quasistationary treatment is adequate to follow the evolution of an SMT binary during this secular phase and calculated the gravitational waveforms. We also pointed out that WDNS observations suggest that there are candidates residing in both regimes.

In the case of tidal disruption (UMT), by contrast, the system will evolve on a hydrodynamical (orbital) time scale. In this scenario the NS may plunge into the WD and spiral into the center of the star, forming a quasiequilibrium configuration that resembles a Thorne-Zytkow object (TZO) [57]; alternatively, the NS may be the receptacle of massive debris from the disrupted WD.

Depending on the details of the EOS, a cold-degenerate gas can support a maximum gravitational mass between $1.65M_\odot$ and $2.2M_\odot$ against catastrophic collapse, if it is not rotating (the TOV limit). It can support 20% more mass, if it is rotating uniformly at the mass-shedding limit (a ''supramassive NS'' [36]), and about 50% more mass, if it rotates differentially (a ''hypermassive NS'' [34–36]). If the total mass of the merged WDNS exceeds the maximum mass supportable by a cold EOS, delayed collapse to a black hole is inevitable after the remnant cools. However, the ultimate fate of the merged WDNS depends on the initial mass of the cold progenitor stars, the degree of mass and angular momentum loss during the WD disruption and binary merger phases, the angular momentum profile of the WDNS remnant and the extent to which the disrupted debris is heated by shocks as it settles onto the NS and forms an extended, massive mantle. These are issues that require a hydrodynamic simulation to resolve. Moreover, ascertaining whether or not the neutron star ultimately undergoes a catastrophic collapse (either prompt or delayed) to a black hole requires that such a simulation be performed in full general relativity. In fact, even the final fate of the NS in the alternative scenario in which there is a long epoch of SMT may also lead to catastrophic collapse, if the neutron star mass is close to the neutron star maximum mass, and this scenario too will require a general relativistic hydrodynamic simulation to track.

In this paper we employ the Illinois adaptive mesh refinement (AMR) relativistic hydrodynamics code [23,58] to perform our first simulations of these alternative scenarios. In particular, we study the head-on collision from rest at large separation of a massive WD and a NS as a prelude to our investigation of the circular binary problem, which we will report in a future work. We focus on compact objects whose total mass exceeds the maximum mass supportable by a cold EOS to determine whether such a collision leads to prompt collapse of the remnant, or a hot gaseous mantle composed of WD debris surrounding a central NS—a Thorne-Zytkow-like object (TZlO).

The vast range of dynamical time scales and length scales involved in this problem make fully general relativistic simulations extremely challenging. For example, a near-Chandrasekhar-mass WD has a radius $R_{\rm WD} \simeq 10^3$ km and dynamical time scale of about 1 s. On the other hand a typical NS has a radius of order $R_{\rm NS} \simeq 10$ km and dynamical time scale of about 1 ms. Therefore, there is a difference of several orders of magnitude both in length scales and time scales. Current numerical relativity techniques and available computational resources make such calculations prohibitive. For this reason, we tackle this problem using a different strategy.

In particular, we construct a piecewise polytropic EOS which captures the main physical features of a NS while, at the same time, scales down the size of the WD. We call these scaled-down WDs ''pseudo-WDs (pWDs).'' We perform a sequence of simulations where we change the EOS so that the pWDs have the same mass ($0.98M_\odot$) but different compactions, while the compaction and mass of the NS involved remain practically unchanged. In other words, while keeping the masses of the binary components and the NS radius fixed, we adjust the ratio of the radius of the pWD to that of the NS so that it varies from 5:1 to 20:1 and then use our results to predict the outcome of the realistic case. The common feature among all versions of the piecewise EOS we employ is that the maximum NS mass always is $1.8M_\odot$ and the maximum WD mass always is $1.43M_\odot$, i.e., the Chandrasekhar mass.

In addition to studying the effects of the pWD compaction, we also study the effects of the NS mass. We consider NSs with masses $1.4M_\odot$ $1.5M_\odot$ and $1.6M_\odot$.

All simulations that we perform show that after the collision, 14%–18% of the initial total rest mass escapes to infinity. The remnant mass in all cases exceeds the maximum rest mass that our *cold* EOS can support ($1.92M_\odot$), but we find that no case leads to prompt collapse to a black hole. This outcome arises because the final configurations are *hot*. All our cases settle into a spherical quasiequilibrium configuration consisting of a cold NS core surrounded by a hot mantle. Hence, all remnants are TZlOs. Extrapolating our results to realistic WD compactions, we predict that the likely outcome of a head-on collision from rest at large separation of a realistic massive WDNS system will be the formation of a quasiequilibrium TZlO.

This paper is organized as follows. In Sec II we review the time scales and length scales involved in a WDNS merger and discuss why this problem presents such a computational challenge. In Sec III we introduce the EOS adopted for our computations and describe our pWD models. Section IV outlines our method for preparing initial data, and Sec V summarizes our methods for evolving the gravitational and matter fields. We present the results of our fully relativistic hydrodynamic simulations in Sec VI, and conclude in Sec VII with a summary of our main findings. Throughout we use geometrized units, where $G = c = 1$.

II. COMPUTATIONAL CHALLENGE

Simulating a WDNS merger in full general relativity is a difficult computational task. In this section we sketch in quantitative terms exactly why this is so.

There are three fundamental time scales and length scales involved in the WDNS merger that must be resolved. The relevant time scales are the dynamical time scale of each component of the binary and the orbital period; the relevant length scales are the NS and WD radii and their orbital separation.

Resolving the WD length scale and dynamical time scale is necessary in order to assess what happens to the WD at merger. Merger occurs on the orbital time scale, so this time scale must also be resolved. Resolving the NS dynamical time scale will enable us to assess whether the NS promptly collapses and forms a black hole, or remains inside the remnant WD, settling into a TZlO.

The dynamical time scale of the NS, $t_{d,\mathrm{NS}}$, is given by

$$t_{d,\mathrm{NS}} = \sqrt{\frac{R_{\mathrm{NS}}^3}{M_{\mathrm{NS}}}}, \tag{1}$$

where R_{NS}, and M_{NS} are the characteristic NS radius and mass, respectively.

Similarly, the dynamical time scale of the WD, $t_{d,\mathrm{WD}}$, is given by

$$t_{d,\mathrm{WD}} = \sqrt{\frac{R_{\mathrm{WD}}^3}{M_{\mathrm{WD}}}}, \tag{2}$$

where R_{WD}, and M_{WD} are the characteristic WD radius and mass, respectively. Finally, the orbital time scale, T, is given by

$$T = 2\pi\sqrt{\frac{A^3}{M_{\mathrm{T}}}}, \tag{3}$$

where $M_{\mathrm{T}} = M_{\mathrm{NS}} + M_{\mathrm{WD}}$ is the total mass, and A is the orbital separation. Note that, at this separation, the head-on collision time scale is

$$T_{\mathrm{coll}} = \frac{\pi}{2\sqrt{2}}\sqrt{\frac{A^3}{M_{\mathrm{T}}}} = \frac{T}{4\sqrt{2}}, \tag{4}$$

assuming the stars free-fall from rest as Newtonian point masses, and hence it is roughly the same order of magnitude as T.

By use of Eqs. (1) and (2) the ratio of the WD time scale to the NS time scale is

$$\frac{t_{d,\mathrm{WD}}}{t_{d,\mathrm{NS}}} = \sqrt{\frac{R_{\mathrm{WD}}^3}{qR_{\mathrm{NS}}^3}}, \tag{5}$$

where

$$q = \frac{M_{\mathrm{WD}}}{M_{\mathrm{NS}}} \tag{6}$$

is the binary mass ratio.

For $M_{\mathrm{WD}} = 1M_\odot$ and using a cold-degenerate electron EOS one finds $R_{\mathrm{WD}} \approx 5000$ km [33,59]. On the other hand, typical NS masses and radii are $M_{\mathrm{NS}} = 1.5M_\odot$, $R_{\mathrm{NS}} \approx 10$ km. Hence, in realistic scenarios the ratio of the WD size to the NS size is

$$\frac{R_{\mathrm{WD}}}{R_{\mathrm{NS}}} \sim 500, \tag{7}$$

and from Eq. (5) the ratio of the dynamical time scales is

$$\frac{t_{d,\mathrm{WD}}}{t_{d,\mathrm{NS}}} \sim 10^4. \tag{8}$$

At the Roche limit, A is typically a few (two to five) times the WD radius [33]. Using, $A \sim 2R_{\mathrm{WD}}$, and the values for the masses and radii used above, the orbital time scale becomes

$$\frac{T}{t_{d,\mathrm{NS}}} = 2\pi\sqrt{\frac{A^3}{(1+q)R_{\mathrm{NS}}^3}} \sim 10^5. \tag{9}$$

It is thus clear that there is a vast range of length scales and time scales involved in this problem. The only way to simulate the WDNS merger is by exploiting the power of adaptive mesh refinement, so that resolution is high only

where required. However, even this does not suffice to tackle the time scale problem as we explain below.

Given that all current numerical relativity schemes for evolving both the spacetime and the fluid are explicit, there are strong limitations imposed on the size of the time step by the Courant-Friedrich-Lewy condition

$$\frac{\Delta t}{\Delta x} = \lambda < C, \tag{10}$$

where λ is the Courant number and C a constant of order unity that depends on the integration scheme employed. If one uses AMR, this implies that the size of the time step has to be different in regions of different mesh size Δx. If we resolve the stars adequately, the mesh size will be much smaller near the NS than near the WD, because in typical scenarios the NS is 500 times smaller than the WD. Equation (10) then implies that the smallest time step must be in the domain of the NS. In particular, if the NS is covered by $N_{\rm NS} = 2R_{\rm NS}/\Delta x_{\rm NS}$ grid zones and the WD is covered by $N_{\rm WD} = 2R_{\rm WD}/\Delta x_{\rm WD}$ grid zones, then from Eq. (10) we have

$$\frac{\Delta t_{\rm WD}}{\Delta t_{\rm NS}} = \frac{\Delta x_{\rm WD}}{\Delta x_{\rm NS}} = \frac{N_{\rm NS}}{N_{\rm WD}} \frac{R_{\rm WD}}{R_{\rm NS}}, \tag{11}$$

where $\Delta t_{\rm NS}$, $\Delta x_{\rm NS}$ and $\Delta t_{\rm WD}$, $\Delta x_{\rm WD}$ denote the time step and mesh size in the vicinity of the NS and WD, respectively.

To assess the potential formation of a black hole requires at least $N_{\rm NS} = 50$ grid zones across the NS, in order that a $2M_\odot$ black hole (BH) [which is a probable mass a BH would have after the merger of a WDNS system of total mass of about $2.5M_\odot$] would be covered by at least 20 grid zones. Even if a BH does not form, covering the NS with 50 grid zones is necessary to reliably model the NS and maintain small Hamiltonian and momentum constraint violations. Resolving the WD requires about $N_{\rm WD} = 30$ grid zones to reliably model the star. If we combine Eq. (7) and (11), we obtain

$$\frac{\Delta t_{\rm WD}}{\Delta t_{\rm NS}} \approx 833. \tag{12}$$

This means that for one time step in the vicinity of the WD we would have to take about 833 time steps in the vicinity of the NS. Even evolving the system for only one WD dynamical time scale would require millions of time steps in the vicinity of the NS. This shows how difficult it is to resolve both the WD and the NS at the same time.

However, what renders the computation of the WDNS merger in full GR prohibitive is that a realistic merger takes place on an orbital time scale, which is equivalent to 10^5 NS dynamical time scales [see Eq. (9)].

To make this quantitative, let us compare the orbital time scale with a typical time step in the vicinity of the NS. Using $N_{\rm NS}$ grid zones across the NS and combining Eq. (1) and (10), we find

$$\frac{t_{d,\rm NS}}{\Delta t_{\rm NS}} = \frac{N_{\rm NS}}{2\lambda}\sqrt{\frac{R_{\rm NS}}{M_{\rm NS}}} \sim 100, \tag{13}$$

where in the last step we used a typical value for the Courant number $\lambda = 0.4$ and the values for $M_{\rm NS}$, $R_{\rm NS}$, $N_{\rm NS}$ we cited above. Combining Eqs. (9) and (13), we obtain

$$\frac{T}{\Delta t_{\rm NS}} \sim 10^7. \tag{14}$$

Hence, a realistic WDNS simulation would require a minimum of 10^7 time steps in the vicinity of the NS. In fact this number of time steps is an underestimate because extracting GWs would require a few orbits and the final system would settle in equilibrium or collapse within a few orbital time scales after merger. As a result, a dynamical, fully general relativistic hydrodynamics WDNS calculation would require of order 10^8 time steps.

We can give an estimate of how long such a simulation would be based on high-resolution (192^3 grid points in the innermost refinement level) benchmark runs we performed for a WDNS system with a $1.5M_\odot$ NS and a $1.0M_\odot$ WD at separation of about $2.7R_{\rm WD}$ (close to the Roche limit), which has an orbital period of about $1.4 \times 10^6 M$, where $M = 2.5M_\odot$. Using 256 cores on the Ranger cluster of the Texas Advanced Computing Center we found that the Illinois GR hydrodynamics code advances about $6M$ per hour. Thus, the entire simulation (of about 10 orbital periods) would require about 264 years of pure computational time.

Realistic WDNS simulations are beyond the capabilities of current computational resources and numerical relativity techniques. For this reason, we will tackle the problem of WDNS mergers and head-on collisions adopting an alternate strategy. We carefully construct an EOS which mimics a realistic cold NS EOS and, at the same time, scales down the size of the WD to make such a calculation feasible. Using sequences of these systems, where the WD size gradually increases, we can extrapolate our results to the realistic case. These scaled-down WDs or pseudo WDs are the subject of the following section.

III. PSEUDO-WHITE DWARFS

In this section we introduce our EOS and describe resulting models for pWDs. Our EOS is the following 6-parameter piecewise polytropic EOS

$$\frac{P}{\rho_0} = \begin{cases} \kappa_1 \rho_0^{1/n_1}, & \rho_0 \le \rho_1 \\ \kappa_2 \rho_0^{1/n_2}, & \rho_1 < \rho_0 \le \rho_2, \\ \kappa_3 \rho_0^{1/n_3}, & \rho_0 > \rho_2 \end{cases} \tag{15}$$

where P is the pressure, ρ_0 is the rest-mass density and κ_1, κ_2, κ_3, n_1, n_2, n_3, ρ_1, ρ_2 are the parameters of the EOS. Note that the parameters are 8 in number but continuity requires that the following conditions be true

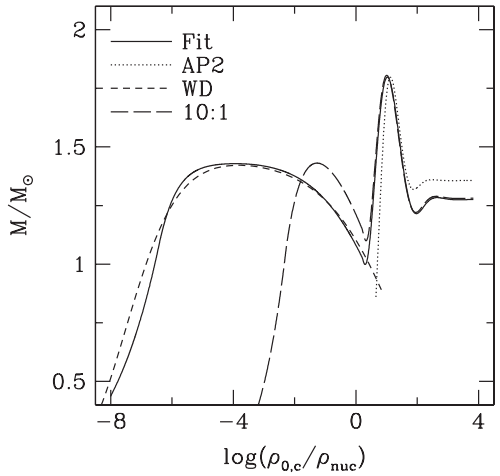

FIG. 1. Mass (M)—central rest-mass density ($\rho_{0,c}$) relationship of single TOV stars for various cold EOSs. In the plot $\rho_{\rm nuc} = 2 \times 10^{14}$ g/cm^3 is the nuclear density. Plotted are the Chandrasekhar electron-degenerate EOS for mean molecular weight per electron $\mu_e = 2$ (labeled as WD), the AP2 version of the Akmal-Pandharipande-Ravenhall EOS [37,60], a polytropic approximation of these realistic EOSs using EOS (15) (labeled as Fit) and a version of EOS (15) where the ratio of the isotropic radius of a $0.98M_\odot$ pWD to the isotropic radius of a $1.5M_\odot$ NS is reduced to ≈ 10 (labeled as 10:1). The parameters of these EOSs are listed in Table I.

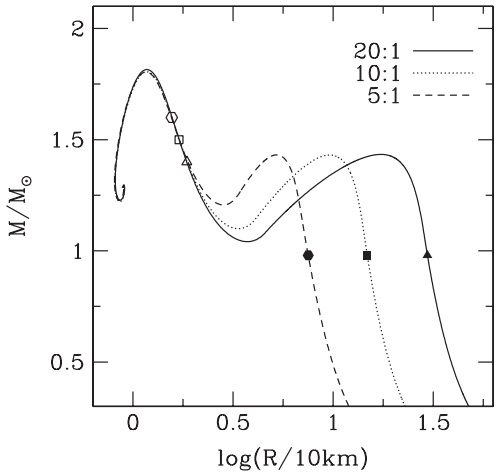

FIG. 2. Mass—radius relationship of TOV stars generated by the piecewise polytropic EOS (15). Plotted are curves corresponding to three versions of the EOS where the ratio of the isotropic radius of a $0.98M_\odot$ pWD to that of a $1.5M_\odot$ NS is 20:1, 10:1 and 5:1. The corresponding EOS parameters are given in Table I. The open points correspond to the NS models studied in this paper, which have masses $1.4M_\odot$, $1.5M_\odot$ and $1.6M_\odot$. The solid points correspond to the pWD models considered in this work, which all have the same mass: $0.98M_\odot$.

$$\kappa_1 = \kappa_2 \rho_1^{1/n_2 - 1/n_1}, \qquad \kappa_2 = \kappa_3 \rho_2^{1/n_3 - 1/n_2}. \tag{16}$$

As a result, the adopted EOS (15) has six free parameters and throughout this paper we use κ_3, n_1, n_2, n_3, ρ_1, ρ_2 to specify an EOS. Note also that we use the polytropic indices n_i instead of the adiabatic indices $\Gamma_i = 1 + 1/n_i$.

The freedom of our multiparameter EOS enables us to capture the same characteristic curves and turning points on a TOV mass-central density plot as for a cold-degenerate realistic EOS (see [59]), as shown in Fig. 1. The figure shows that EOS (15) can provide a reasonable approximation to the mass-central density relation of realistic compact objects, exhibiting both stable ($dM/d\rho_{0,c} > 0$) and unstable ($dM/d\rho_{0,c} < 0$) branches for both WDs and NSs.

Furthermore, EOS (15) allows us to adjust the size of a pWD of given mass, thereby shifting the pWD branch to smaller radii (see Fig. 2), while keeping the NS masses and radii approximately unchanged for $M_{\rm NS} \geq 1.3M_\odot$. The shifted branches in Fig. 2 correspond to the stars that we call pseudo-WDs in this work.

Finally, note that all versions of EOS (15) considered in this work have been carefully constructed so that the maximum gravitational mass of a NS is $1.8M_\odot$, i.e., the same as that for the AP2 version of the Akmal-Pandharipande-Ravenhall EOS [37,60], and the maximum gravitational mass of a pWD is $1.43M_\odot$, i.e., the maximum mass of a TOV WD obeying the Chandrasekhar EOS for $\mu_e = 2$. In addition, EOS (15) is constructed to preserve the shape of the M vs $\rho_{0,c}$ curve, yielding both stable and unstable branches and turning points appropriately.

IV. INITIAL DATA

In this section we present the basic formalism for generating valid general relativistic initial data for the head-on collision in a given pWDNS system.

A. Gravitational field equations

We begin by writing the spacetime metric in the standard 3 + 1 form [61]

$$ds^2 = -\alpha^2 dt^2 + \gamma_{ij}(dx^i + \beta^i dt)(dx^j + \beta^j dt), \tag{17}$$

where α is the lapse function, β^i the shift vector and γ_{ij} the three-metric on spacelike hypersurfaces of constant time t. Throughout the paper Latin indices run from 1 to 3, whereas Greek indices run from 0 to 3.

We conformally decompose the three-metric γ_{ij} as

$$\gamma_{ij} = \Psi^4 f_{ij}, \tag{18}$$

where Ψ is the conformal factor and f_{ij} the conformal metric. We adopt the standard approximation of a conformally flat spacetime, so that $f_{ij} = \delta_{ij}$ in Cartesian coordinates.

Since we are interested in head-on collisions between compact objects, we assume that initially the stars begin to accelerate towards each other starting from rest. As a result the extrinsic curvature is initially zero and the momentum

TABLE I. Parameters for the piecewise polytropic EOS (15) used in generating different stellar models. The first column corresponds to the name of the EOS. An EOS named M:N corresponds to a version of (15) for which the mass—radius relationship of TOV stars is such that the ratio of the isotropic radius of a $0.98M_\odot$ pWD to that of a $1.5M_\odot$ NS is M:N (see Fig. 2). The EOS named AP2 is the same as the AP2 EOS defined in [60]. Finally, the EOS named Fit is an approximate fit to the Chandrasekhar EOS (for $\mu_e = 2$) joined onto the AP2 EOS (see Fig. 1). Here $\rho_{\rm nuc} = 1.48\,494 \times 10^{-4}$ km^{-2} and κ_3 is given in geometrized units.

EOS name	κ_3	n_1	n_2	n_3	$\log(\rho_1/\rho_{\rm nuc})$	$\log(\rho_2/\rho_{\rm nuc})$
20:1	5064.2599	1.56 128	2.98 418	0.714 286	−3.17 219	0.180 473
10:1	4993.0688	1.51 515	2.96 971	0.714 286	−2.26 862	0.208 502
5:1	6123.5567	1.51 883	2.94 291	0.699 301	−1.2909	0.267 623
AP2	145 414.043	0.60 864	0.49 652	0.514 139	0.398 915	0.698 922
Fit	4458.0491	2.	2.96 736	0.716	−6.39 356	0.208 502

constraints are identically satisfied [62]. Hence, we need only prepare initial data for Ψ.

Under the aforementioned assumptions the only equation we have to solve is the Hamiltonian constraint, which becomes

$$\nabla^2\Psi = -2\pi\Psi^5\rho, \tag{19}$$

where ∇^2 is the flat Laplacian operator. Here the source term ρ is defined as

$$\rho \equiv n^\alpha n^\beta T_{\alpha\beta}, \tag{20}$$

and where n^α is the normal vector to a $t =$ constant slice, and $T_{\alpha\beta}$ is the stress-energy tensor of the matter.

The gauge is chosen so that the initial slice is maximal, i.e., $K = 0$ and $\partial_t K = 0$, and the shift vector is set equal to zero. Using the assumption of maximal slicing it is straightforward to derive an equation for the lapse [11,63]

$$\nabla^2\tilde{\alpha} = 2\pi\tilde{\alpha}\Psi^4(\rho + 2S), \tag{21}$$

where

$$\tilde{\alpha} = \alpha\Psi, \tag{22}$$

and the source term S is defined as

$$S \equiv \gamma^{ij}T_{ij}. \tag{23}$$

Eqs. (19) and (21) are elliptic and hence have to be supplemented with outer boundary conditions. Following [63], we impose $1/r$ falloff conditions on $\alpha - 1$ and $\Psi - 1$ at the outer boundary.

B. Matter fields

To model the matter, a perfect fluid stress-energy tensor is assumed:

$$T^{\alpha\beta} = (\rho_0 + \rho_i + P)u^\alpha u^\beta + Pg^{\alpha\beta}, \tag{24}$$

where $g^{\alpha\beta}$ is the inverse of the four-metric and ρ_0, ρ_i, P, u^α are the rest-mass density, internal energy density, pressure, and four-velocity of the fluid, respectively.

Since the initial configuration is assumed to be at rest in the center of mass frame, the initial fluid four-velocity is given by

$$u^\alpha = u^t(1, 0, 0, 0) \tag{25}$$

or

$$u^\alpha = \alpha u^t n^\alpha. \tag{26}$$

A straightforward calculation shows that the source term ρ in Eq. (20) can then be written as

$$\rho = \rho_0 + \rho_i, \tag{27}$$

and S in Eq. (23) as

$$S = 3P. \tag{28}$$

C. Computational methods

To solve the elliptic Eqs. (19) and (21) we developed a fixed-mesh-refinement (FMR) finite difference code based on the Portable, Extensible Toolkit for Scientific Computation (PETSc) algorithms [64–66]. The grid structure used in our code is a multilevel set of properly nested, cell-centered uniform grids. We use a standard second-order finite difference stencil for the Laplacian operator and first-order interpolation across the refinement level boundaries. The nonlinearity of Eq. (19) is addressed by performing Newton-Raphson iterations. A brief description of our FMR implementation is summarized in Appendix A, to which we refer the interested reader.

1. Diagnostics

To check the consistency of solutions obtained with our FMR code we calculate the following diagnostic quantities:

The Arnowitt-Deser-Misner (ADM) mass is given by

$$M_{\rm ADM} = -\frac{1}{2\pi}\oint_\infty \partial^i\Psi dS_i = -\frac{1}{2\pi}\int \nabla^2\Psi d^3x, \tag{29}$$

where we have applied Gauss' theorem to convert the surface integral into a volume integral. The actual expression we use to calculate the ADM mass volume integral is (29) with $\nabla^2\Psi$ replaced by the right-hand side of Eq. (19).

The Komar mass is given by

$$M_{\rm K} = \frac{1}{4\pi}\oint_{\infty} \partial^i \alpha dS_i = \frac{1}{4\pi}\int \nabla^2 \alpha d^3x, \qquad (30)$$

where again we have applied Gauss' theorem in the last step. By use of Eqs. (19) and (21) we find

$$\nabla^2\alpha = -\frac{2}{\Psi}\nabla_i\alpha\nabla^i\Psi + 4\pi\alpha\Psi^4(\rho + S). \qquad (31)$$

The actual expression we use to calculate the Komar mass volume integral is (30) with $\nabla^2\alpha$ replaced by the right-hand side of Eq. (31).

Finally, the total baryon mass is given by [63]

$$M_0 = \int_{\mathcal{M}} \rho_o \alpha u^t \Psi^6 d^3x, \qquad (32)$$

where $\mathcal{M}$ means that the integration is carried over the support of the matter.

2. Code Testing

Gauss' theorem constitutes a strong consistency check for our FMR code. To demonstrate that the solutions obtained with our elliptic code satisfy Gauss' theorem and achieve second-order convergence we performed the following test. Employing the 10:1 piecewise polytropic EOS we constructed TOV NS solutions of various masses with a 1D TOV integrator. We then used second-order polynomial interpolation to set up the rest-mass density profiles in our FMR elliptic code and solve Eqs. (19) and (21) for the conformal factor and lapse function. We set up grids with five levels of refinement ($nl = 5$) centered on the NS, and three different resolutions $nx = ny = nz = 32$, $\Delta x_5 = 2.2$ km, $nx = ny = nz = 64$, $\Delta x_5 = 1.1$ km and $nx = ny = nz = 128$, $\Delta x_5 = 0.55$ km. In Fig. 3 we demonstrate that our numerical solutions satisfy Gauss' theorem, are in agreement with the TOV integration, and that our code is second-order convergent for this test. To generate the plot we used the results of the ADM mass integration but the convergence properties remain the same when we use the results of the Komar mass integration.

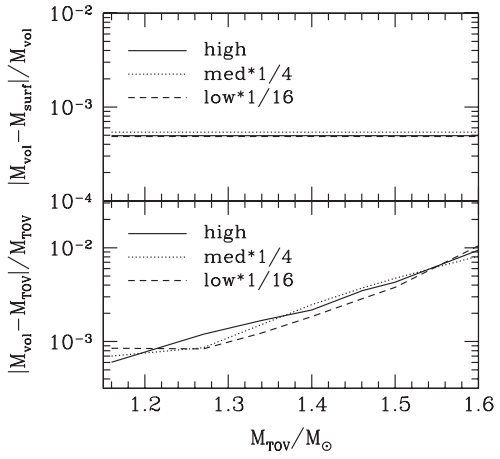

FIG. 3. Convergence test for the FMR elliptic code using TOV stars. Five levels of refinement have been used for this test. Upper panel: Fractional difference between the volume integral $M_{\rm vol}$ and surface integral $M_{\rm surf}$ for the ADM mass, calculated with our FMR elliptic code, versus the gravitational mass $M_{\rm TOV}$ calculated with a 1D integrator of the TOV equations. The plot demonstrates satisfaction of Gauss' theorem and second-order convergence. Lower panel: Fractional difference between $M_{\rm vol}$ and $M_{\rm TOV}$ versus $M_{\rm TOV}$. The plot demonstrates equality of $M_{\rm vol}$ and $M_{\rm TOV}$ and second-order convergence of our FMR elliptic code to the 1D (exact) result. In both panels three resolutions are plotted: low $\equiv 32^3$, med $\equiv 64^3$, high $\equiv 128^3$. Resolutions 32^3 and 64^3 have been rescaled with a factor of 1/16 and 1/4 respectively, so that they overlap with resolution 128^3.

V. EVOLUTION OF WDNS SYSTEMS

A. Basic equations

The formulation and numerical scheme for our simulations are the same as those already reported in [22,58,67], to which the reader may refer for details. Here we introduce our notation and summarize our method.

We use the 3 + 1 formulation of general relativity where the metric is decomposed in the form of Eq. (17), and where the fundamental dynamical variables for the metric evolution are the spatial three-metric γ_{ij} and extrinsic curvature K_{ij}. We adopt the Baumgarte-Shapiro-Shibata-Nakamura (BSSN) formalism [11,68,69], in which the evolution variables are the conformal exponent $\phi \equiv \ln(\gamma)/12$, the conformal three-metric $\tilde{\gamma}_{ij} = e^{-4\phi}\gamma_{ij}$, three auxiliary functions $\tilde{\Gamma}^i \equiv -\tilde{\gamma}^{ij}{}_{,j}$, the trace of the extrinsic curvature K, and the trace-free part of the conformal extrinsic curvature $\tilde{A}_{ij} \equiv e^{-4\phi}(K_{ij} - \gamma_{ij}K/3)$. Here, $\gamma = \det(\gamma_{ij})$. The full spacetime metric $g_{\mu\nu}$ is related to the three-metric $\gamma_{\mu\nu}$ by $\gamma_{\mu\nu} = g_{\mu\nu} + n_\mu n_\nu$, where the future-directed, timelike unit vector n^μ normal to the time slice can be written in terms of the lapse α and shift β^i as $n^\mu = \alpha^{-1}(1, -\beta^i)$. The evolution equations of these BSSN variables are given by Eqs. (9)–(13) in [22].

We adopt standard puncture gauge conditions: an advective "1 + log" slicing condition for the lapse and a "Gamma-freezing" condition for the shift [70]. Thus, we have

$$\partial_0\alpha = -2\alpha K, \qquad (33)$$

$$\partial_0\beta^i = (3/4)B^i, \qquad (34)$$

$$\partial_0 B^i = \partial_0\tilde{\Gamma}^i - \eta B^i, \qquad (35)$$

where $\partial_0 \equiv \partial_t - \beta^j\partial_j$. We set the η parameter to 0.01 km^{-1} for all simulations presented in this work.

The fundamental matter variables are the rest-mass density ρ_0, specific internal energy ϵ, pressure P, and four-velocity u^μ. We write the stress-energy tensor as

$$T_{\mu\nu} = \rho_0 h u_\mu u_\nu + P g_{\mu\nu}, \tag{36}$$

where $h = 1 + \epsilon + P/\rho_0$ is the specific enthalpy and ϵ is the total energy density. In our numerical implementation of the hydrodynamics equations, we evolve the "conservative" variables ρ_*, $\tilde{S}_i$, and $\tilde{\tau}$. They are defined as

$$\rho_* \equiv -\sqrt{\gamma}\rho_0 n_\mu u^\mu, \tag{37}$$

$$\tilde{S}_i \equiv -\sqrt{\gamma} T_{\mu\nu} n^\mu \gamma^\nu{}_i, \tag{38}$$

$$\tilde{\tau} \equiv \sqrt{\gamma} T_{\mu\nu} n^\mu n^\nu - \rho_*. \tag{39}$$

The evolution equations for these variables are given by Eqs. (21)–(24) in [22].

The EOS we adopt for the evolution has both a thermal and cold contribution, i.e.,

$$P = P_{\rm th} + P_{\rm cold}, \tag{40}$$

where $P_{\rm cold}$ is given by Eq. (15) and the thermal pressure is given by

$$P_{\rm th} = (\Gamma_{\rm th} - 1)\rho_0(\epsilon - \epsilon_{\rm cold}), \tag{41}$$

where

$$\epsilon_{\rm cold} = -\int P_{\rm cold} d(1/\rho_0). \tag{42}$$

We set $\Gamma_{\rm th} = 1.66$ ($\simeq 5/3$) in all our simulations, i.e., we set it equal to the Γ_1 exponent of the 10:1 EOS, appropriate either for nonrelativistic cold-degenerate electrons or (shock) heated, ideal nondegenerate baryons. Equation (40) reduces to our piecewise polytropic law Eq. (15) for the initial (cold) NS and pWD matter.

B. Evolution of the metric and hydrodynamics

We evolve the BSSN equations using fourth-order accurate, centered finite-differencing stencils, except on shift advection terms, where fourth-order accurate upwind stencils are applied. We apply Sommerfeld outgoing wave boundary conditions on all BSSN fields, as in [22]. Our code is embedded in the CACTUS parallelization framework [71], and our fourth-order Runge-Kutta time stepping is managed by the MoL (method of lines) thorn, with the Courant-Friedrich-Lewy number set to 0.45 in all pWDNS simulations. We use the CARPET [72] infrastructure to implement the moving-box adaptive mesh refinement. In all AMR simulations presented here, we use second-order temporal prolongation, coupled with fifth-order spatial prolongation, and impose equatorial symmetry to reduce the computational cost.

We write the general relativistic hydrodynamics equations in conservative form. They are evolved via a high-resolution shock-capturing technique [58,67] that employs the piecewise parabolic (PPM) reconstruction scheme [73], coupled to the Harten, Lax, and van Leer approximate Riemann solver [74]. The adopted hydrodynamic scheme is second-order accurate. To stabilize our hydrodynamic scheme in regions where there is no matter, a tenuous atmosphere is maintained on our grid, with a density floor $\rho_{\rm atm}$ set to 10^{-10} times the initial maximum density on our grid. The initial atmospheric pressure $P_{\rm atm}$ is set by using the cold EOS (15). Throughout the evolution, we impose limits on the pressure to prevent spurious heating and negative values of the internal energy ϵ. Specifically, we require $P_{\rm min} \le P \le P_{\rm max}$, where $P_{\rm max} = 10P_{\rm cold}$ and $P_{\rm min} = 0.8P_{\rm cold}$, where $P_{\rm cold}$ is the pressure calculated using the cold EOS (15). Whenever P exceeds $P_{\rm max}$ or drops below $P_{\rm min}$, we reset P to $P_{\rm max}$ or $P_{\rm min}$, respectively. Following [75] we impose the upper pressure limits only in regions where the rest-mass density remains very low ($\rho_0 < 100\rho_{\rm atm}$), but we impose the lower limit everywhere on our grid.

At each time step, the "primitive variables" ρ_0, P, and v^i must be recovered from the conservative variables ρ_*, $\tilde{\tau}$, and $\tilde{S}_i$. We perform the inversion numerically as specified in [58]. We use the same technique as in [22] to ensure that the values of $\tilde{S}_i$ and $\tilde{\tau}$ yield physically valid primitive variables, except we reset $\tilde{\tau}$ to $10^{-10}\tilde{\tau}_{0,\rm max}$ (where $\tilde{\tau}_{0,\rm max}$ is the maximum value of $\tilde{\tau}$ initially) when either $\tilde{S}_i$ or $\tilde{\tau}$ is unphysical [i.e., violate one of the inequalities (34) or (35) in [22]]. The restrictions are usually imposed only in the low-density atmosphere.

It is instructive to discuss the mathematical structure of the system of hydrodynamic equations when a piecewise polytropic EOS (15) is used. According to [76,77], when the fluxes of the conservation laws are nonsmooth, split waves and composite structures may be present in the solutions. In these cases a numerical solution may not converge to the correct solution. In our case the fluxes are not smooth everywhere because EOS (15) is nonsmooth (it is continuous but not differentiable) at the turning points ρ_i, $i = 1, 2$. Away from the turning points the fluxes are smooth, therefore there may be some concern when nonlinear waves cross the transition densities. However, according to [77] our adopted numerical scheme should be able to handle such composite structures, if they ever arise, and our solutions should converge to the correct continuum solution.

To study this effect we constructed an EOS which is similar to Eq. (15), but where the pressure discontinuities are "smoothed out" at the turning points ρ_i, ($i = 1, 2$), such that the EOS becomes a smooth, once (or twice) differentiable function of the rest-mass density. We perform such a smoothing operation using a cubic (or quintic) spline over a density interval $[\rho_i(1 - \epsilon), \rho_i(1 + \epsilon)]$, where $\epsilon > 0$. We chose ϵ to be sufficiently small so that the smoothed EOS mimics as closely as possible EOS (15), but large enough to avoid roundoff errors due to very large gradients. Setting up several generalized Riemann problems, we found that the numerical solutions obtained using EOS (15) converge to those obtained when using its

smooth counterpart and the two can hardly be distinguished for the resolutions considered. Therefore, our numerical schemes in conjunction with EOS (15) are able to capture the correct solution, in that they are almost identical to the solutions obtained with the smooth counterpart of (15). For the details of this analysis, we refer the interested reader to Appendix B.

C. Evolution diagnostics

During the evolution, we monitor the normalized Hamiltonian and momentum constraints as defined in Eqs. (40)–(43) of [22].

We also monitor the ADM mass and angular momentum of the system, which can be calculated during the evolution by surface integrals at a large distance (Eqs. (37) and (39) of [22]). The equations used to calculate the ADM mass and angular momentum with minimal numerical noise are as follows [11]:

$$M = \int_V d^3x \Big(\psi^5 \rho + \frac{1}{16\pi} \psi^5 \tilde{A}_{ij} \tilde{A}^{ij} - \frac{1}{16\pi} \tilde{\Gamma}^{ijk} \tilde{\Gamma}_{jik} + \frac{1-\psi}{16\pi} \tilde{R} - \frac{1}{24\pi} \psi^5 K^2 \Big), \tag{43}$$

$$J_i = \frac{1}{8\pi} \epsilon^n_{ij} \int_V d^3x \Big[\psi^6 \Big(\tilde{A}^j_n + \frac{2}{3} x^j \partial_n K - \frac{1}{2} x^j \tilde{A}_{km} \partial_n \tilde{\gamma}^{km} \Big) + 8\pi x^j S_n \Big]. \tag{44}$$

Here V is the volume within a distant surface, $\psi = e^{\phi}$, $\rho = n_\mu n_\nu T^{\mu\nu}$, $S_i = -n_\mu \gamma_{i\nu} T^{\mu\nu}$, $\tilde{R}$ is the Ricci scalar associated with $\tilde{\gamma}_{ij}$, and $\tilde{\Gamma}_{ijk}$ are Christoffel symbols associated with $\tilde{\gamma}_{ij}$.

In this work we only focus on head-on collisions, so there is no angular momentum involved. However, our simulations are three-dimensional, so there is no guarantee that J_i will remain 0. In order to quantify violations of $J_i = 0$ we normalize the angular momentum, computed via (44), with the angular momentum a pWDNS system would have, if the binary components were Newtonian point masses in circular orbit at the initial separation A, i.e.,

$$J_{z,c} = M_{\rm T}^{3/2} A^{1/2} \frac{q}{(1+q)^2}, \tag{45}$$

where the total mass $M_{\rm T}$ is taken to be the sum of ADM masses of the isolated stars.

When hydrodynamic matter is evolved on a fixed uniform grid, our hydrodynamic scheme guarantees that the rest mass M_0 is conserved to machine roundoff error. This strict conservation is no longer maintained in an AMR grid, where spatial and temporal prolongation is performed at the refinement boundaries. Hence, we also monitor the rest mass

$$M_0 = \int \rho_* d^3x \tag{46}$$

during the evolution. Rest-mass conservation is also violated whenever ρ_0 is reset to the atmosphere value. This usually happens only in the very low-density atmosphere. The low-density regions do not affect rest-mass conservation significantly.

Shocks occur when stars collide. We measure the entropy generated by shocks via the quantity $K \equiv P/P_{\rm cold} \geq 1$, where $P_{\rm cold}$ is the pressure associated with the cold EOS that characterizes the initial matter [see Eq. (15)].

VI. CASES AND RESULTS

A. Initial configurations

We perform a number of pWDNS head-on collision simulations varying the initial configurations, so that we can study the effect of the pWD compaction and NS mass on the final outcome separately. Table II outlines the physical parameters for the cases considered in this work, and Table III presents the AMR grid structure used in each case.

To generate initial data for our cases we first choose the ADM mass $M_{\rm NS}$ of the NS and the ADM mass $M_{\rm WD}$ of the pWD (see Table II) and solve the TOV equations for each

TABLE II. Summary of initial configurations. $M_{\rm NS}$ ($M_{\rm WD}$) stands for the ADM mass of an isolated NS (pWD)[a], $R_{\rm NS}$ ($R_{\rm WD}$) is the isotropic radius of an isolated NS (pWD), $C_{\rm NS}$ ($C_{\rm WD}$) is the compaction of an isolated NS (pWD), where the compaction is defined as the ratio of the ADM mass of the isolated star to its areal radius. $M_{\rm ADM}$ is the ADM mass of the system and A the initial binary separation in isotropic coordinates. All cases have exactly the same coordinate separation of 586.9 km to allow for comparison. Cases A1, A2, A3 have been produced with the 10:1 EOS, while cases B and C have been produced with the 5:1 and 20:1 EOSs, respectively.

Case	$M_{\rm NS}/M_\odot$	$M_{\rm WD}/M_\odot$	$C_{\rm NS}$	$C_{\rm WD}$	$R_{\rm WD}/R_{\rm NS}$	$R_{\rm WD}/M_{\rm ADM}$	$M_{\rm ADM}/M_\odot$	$A/R_{\rm WD}$
A1	1.4	0.98	0.111	0.010	8.88	41.18	2.413	4.000
A2	1.5	0.98	0.130	0.010	9.96	39.36	2.524	4.000
A3	1.6	0.98	0.151	0.010	11.15	37.46	2.652	4.000
B	1.5	0.98	0.130	0.019	4.99	19.76	2.524	7.967
C	1.5	0.98	0.130	0.005	20.01	79.08	2.524	1.991

[a]Here we list the ADM masses, isotropic radii and compactions of the isolated (TOV) stars whose rest-mass density profiles we used to generate initial data for Ψ and α for a given case.

TABLE III. Grid configurations used in our simulations. Here M is the sum of the ADM masses of the isolated stars, Max. res. is the grid spacing in the innermost refinement box surrounding the NS, $N_{\rm NS}$ denotes the number of grid points covering the diameter of the NS initially, and $N_{\rm WD}$ denotes the number of grid points covering the diameter of the pWD initially. The smallest outer boundary distance corresponds to case A3 and is $1028M$.

Case	$M/M_\odot$	Grid hierarchy (in units of M)[a]	Max. res.	$N_{\rm NS}$	$N_{\rm WD}$
A1	2.38	(534.33, 267.16, 133.58, 66.79, 35.78[N/A], 19.08[N/A], 10.44[N/A], 7.156[N/A])	$M/6.71$	63	35
A2a	2.48	(510.62, 255.31, 127.65, 63.83, 34.81[N/A], 18.86[N/A], 10.15[N/A], 6.890[N/A])	$M/5.52$	44	28
A2b	2.48	(534.33, 267.16, 133.58, 66.79, 35.78[N/A], 19.08[N/A], 10.44[N/A], 7.156[N/A])	$M/6.71$	56	35
A3	2.58	(467.27, 233.64, 116.82, 58.41, 29.20 [N/A], 15.58[N/A], 8.518[N/A], 5.841[N/A])	$M/8.22$	56	38
B	2.48	(534.33, 267.16, 133.58, 66.79, 35.78[31.93], 19.08[N/A], 10.44[N/A], 7.156[N/A])	$M/6.71$	56	35
C	2.48	(534.33, 267.16, 133.58, 66.79[N/A], 35.78[N/A], 19.08[N/A], 10.44[N/A], 7.156[N/A])	$M/6.71$	56	35

[a]There are two sets of nested refinement boxes: one centered on the NS and one on the pWD. This column specifies the half side length of the refinement boxes centered on both the NS and pWD. When the side length around the pWD is different, we specify the pWD half side length in square brackets. When there is no corresponding pWD refinement box (as the pWD is much larger than the NS), we write [N/A] for that box.

star in isotropic coordinates to prepare the rest-mass density distribution for the NS and the pWD separately. We then use second-order polynomial interpolation to interpolate the rest-mass density profiles onto the nested grids of our FMR elliptic initial value code and solve Eqs. (19) and (21) for Ψ and α. The two stars are placed at coordinate separation A and such that the Newtonian center of mass of the system is identified with the origin of the coordinate system. Once a solution is achieved by the FMR code for the initial metric, we map ρ_0, Ψ and α from the elliptic code grids onto the evolution grids using second-order polynomial interpolation. We always make sure that the resolution of the initial data grids is higher than the resolution of the evolution grids. The surfaces of the stars are a locus of rapidly decreasing density gradients. As a result, small oscillations due to interpolation may arise and lead to negative rest-mass density. To cure this, we set the density ρ_0 equal to the tenuous atmosphere density that we maintain on the grid whenever $|\rho_0/\rho_{i,c}| < 10^{-10}$, where ρ_0 is the value of the density after the interpolation and $\rho_{i,c}$, $i =$ WD, NS, is the central density of the WD or NS. We do not find such oscillations when interpolating the gravitational fields, which is most likely due to the fact that these are sufficiently smooth.

In all cases we require that the sum of the ADM masses of the isolated stars be larger than the maximum gravitational mass of $1.8M_\odot$ that our cold EOS can support (see Fig. 2). There exist at least 18 observed WDNS systems that satisfy this requirement. Since typical NS and WD masses in massive WDNS binaries lie in the range $1.3M_\odot$–$1.6M_\odot$ and $0.5M_\odot$–$1.1M_\odot$ respectively (see Sec. I), we choose pWD rest-mass density profiles that correspond to an ADM mass of $0.98M_\odot$ in isolation and keep it fixed in all cases we study. This almost fixes the pWD rest mass, because of the small compaction (< 0.02) of the pWDs we consider. The pWD rest-mass variation from case B to case C, due to fixing the ADM mass, is 0.7%. We vary only the pWD compaction, i.e., the EOS, and the NS mass. The reason why we chose the pWD mass to be $0.98M_\odot$ is that the ratio of the isotropic radius of a pWD of such mass to the isotropic radius of a $1.5M_\odot$ NS is ≈ 10 for the 10:1 EOS.

Another quantity that we fix in all our simulations is the initial coordinate separation A of the two components. This almost fixes the kinetic energy of the stars when they collide. In particular, we set $A = 4R_{\rm WD,A}$. Here $R_{\rm WD,A}$ denotes the isotropic radius of the spherical $0.98M_\odot$ pWD used in cases A1, A2, A3. We choose the initial separation this way because we want the stars to be sufficiently far apart so that spherical TOV initial models remain in near equilibrium, and at the same time, simulate the collision within reasonable time scales, as the head-on collision time scale varies as $\sim A^{3/2}$ [see Eq. (4)].

If $A = 4R_{\rm WD,A}$, the NS tidal field in the vicinity of the pWD is small, validating our assumption that an equilibrium pWD is nearly spherical. To see this, let us calculate the ratio of the tidal force of the NS on the surface of the pWD to the surface gravity of the pWD

$$\frac{F^{\rm t}_{\rm NS}}{F_{\rm WD}} = \frac{M_{\rm NS}}{M_{\rm WD}}\left(\frac{R_{\rm WD,A}}{A}\right)^3 \simeq 5\%, \tag{47}$$

where we used $M_{\rm NS} = 1.5M_\odot$, $M_{\rm WD} = 1M_\odot$, $A = 3R_{\rm WD,A}$. Hence, any deviations from sphericity should be small. The assumption of sphericity for case B is even better because in this case $A \approx 8R_{\rm WD,B}$, but worse for case C, where $A \approx 2R_{\rm WD,C}$. In principle, we could increase the separation so that the sphericity approximation becomes better for all cases, but if the final remnant does not collapse promptly to form a BH starting at close separations, it is unlikely that it will collapse if the initial separation is larger. This is due to the fact that for larger separations the kinetic energy at collision will be larger, generating more shock heating that will work to prevent prompt collapse.

To summarize, the set of cases A1, A2, and A3 probe the effect of the NS mass on the final outcome, whereas the set of cases A2, B, and C probe the effect of the pWD

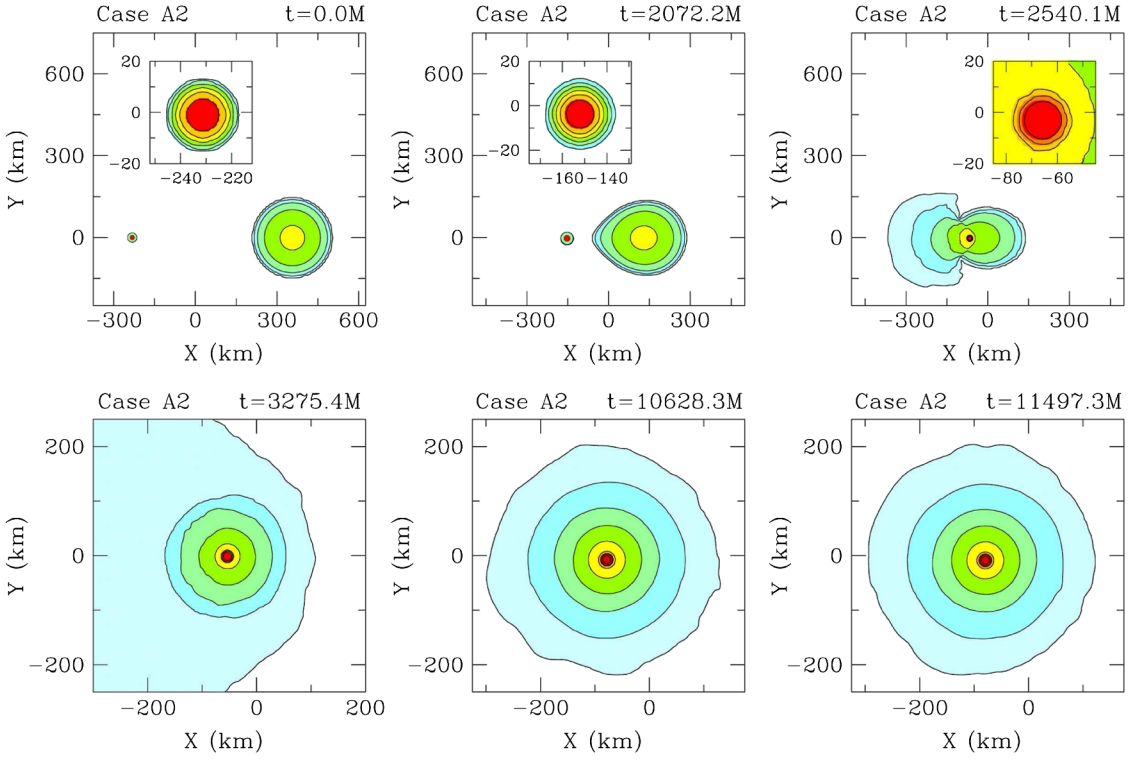

FIG. 4 (color online). Snapshots of rest-mass density profiles at selected times for case A2. The contours represent the rest-mass density in the orbital plane, plotted according to $\rho_0 = \rho_{0,\max} 10^{-0.66j-0.16} (j = 0, 1, \ldots, 9)$. The color sequence dark red, red, orange, yellow, green, light green, blue, and light blue implies a sequence from higher to lower values. This roughly corresponds to darker grey scaling for higher values. The maximum initial NS density is $\rho_{0,\max} = 4.6454 \rho_{\rm nuc}$. The last two snapshots are near the end of the simulation, and they demonstrate that the density contours within a radius of about 150 km remain unchanged. Here $M = 2.48 M_\odot = 3.662$ km $= 1.222 \times 10^{-5}$ s is the sum of the ADM masses of the isolated stars.

compaction on the final outcome. In the following sections we summarize the results of our simulations.

B. Dynamics of collision and effects of the NS mass

Here we describe the effects of the NS mass on the dynamics of pWDNS head-on collisions. We find that about 18% of the initial total mass escapes to infinity for all cases A1, A2, and A3. Nevertheless, the initial total mass in these cases is large enough to guarantee that the final total mass of the pWDNS remnant still exceeds the maximum mass that our cold EOS can support. However, prompt collapse to a black hole does not take place in any of the cases studied because strong shock heating gives rise to a hot remnant. Ultimate collapse to a BH is almost certain after the remnant has cooled. The outcome of the three cases A1, A2, A3 is a TZlO.

Overall, cases A1, A2, and A3 are qualitatively similar and for this reason we mainly describe case A2 as representative of this class of our simulations. Furthermore, our study of case A2 with two different resolutions (see Table III) shows the results to be qualitatively insensitive to resolution indicating that the resolutions used in our simulations are sufficiently high. In what follows all case A2 plots correspond to the high-resolution run of case A2, i.e., case A2b.

In general, the head-on collision of pWDNS systems can be decomposed into three phases: the acceleration, the plunge, and the quasiequilibrium phase.

During the acceleration phase, the two stars accelerate toward one another starting from rest. The separation

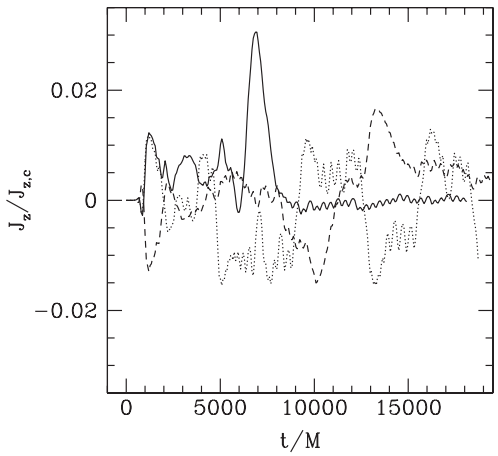

FIG. 5. Normalized angular momentum vs time. J_z and $J_{z,c}$ are given by Eqs. (44) and (45), respectively. The solid, dashed and dotted lines correspond to cases A2, B, and C, respectively. Here $M = 2.48 M_\odot = 3.662$ km $= 1.222 \times 10^{-5}$ s.

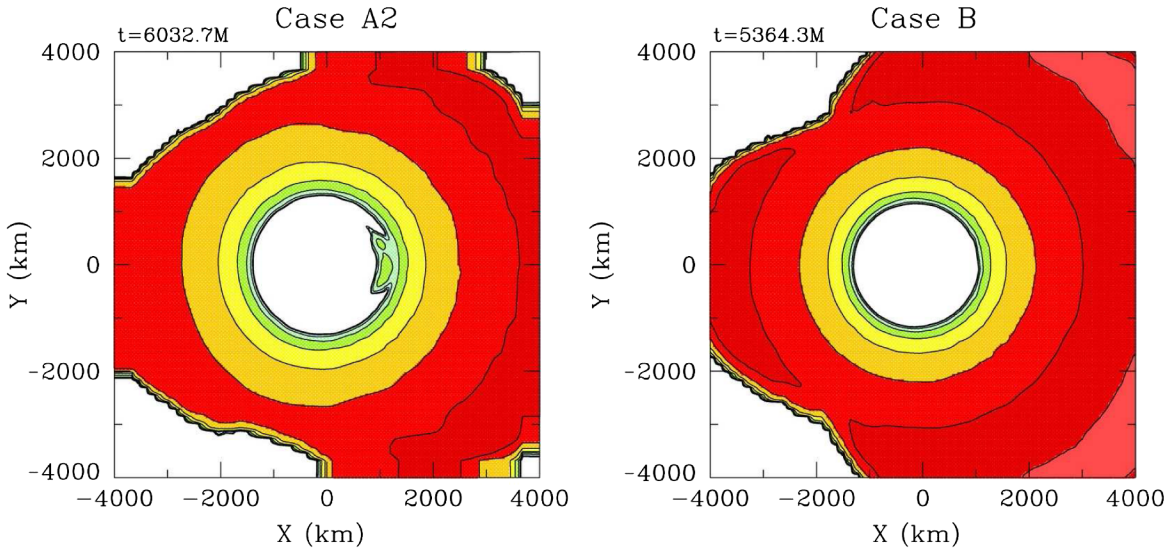

FIG. 6 (color online). Snapshot of total energy per unit mass $U = -u_0 - 1$ (subtracting the rest-mass energy) for cases A2 and B, when matter has already started crossing the outer boundary of the computational domain. Matter with $U < 0$ is bound, while $U > 0$ implies that matter is unbound. The contours represent the total energy per unit mass in the equatorial plane, plotted according to $U = U_{\rm min}10^{0.37j} (j = 0, 1, \ldots, 9)$. The color code here is the same as that defined in Fig. 4. The white spaces in the centers of the plots correspond to bound matter ($U < 0$). We chose the cutoff value $U_{\rm min} = 10^{-4}$. The size of the bound matter area is insensitive to the choice of $U_{\rm min}$. Here $M = 2.48 M_\odot = 3.662$ km $= 1.222 \times 10^{-5}$ s.

decreases as a function of time and this phase ends when the two stars first make contact.

As the separation decreases, the increasing NS tidal field strongly distorts the pWD. This can be seen in the equatorial rest-mass density contours of Fig. 4. In the insets of Fig. 4, the NS interior is almost unchanged during this phase. In reality, it oscillates but is not tidally distorted by the pWD. Nevertheless, the NS atmosphere does expand. The insets also show that due to numerical errors the NS veers slightly off the x-axis, which is the collision axis in our simulations. In general, in all our simulations both the NS and the pWD wiggle around the x-axis. The amplitude of the NS wiggling motion is at most 1% of the pWD radius, while the amplitude of the pWD off-axis motion is less than 0.1% of its radius. Hence, the collision is practically head-on.

It is likely that this lack of symmetry is due to small asymmetries introduced when mapping the initial data onto the evolution grids via second-order interpolation. This is because second-order interpolation requires the use of 3 grid points (per direction) that surround the point to which one interpolates. However, the effect is small and our results cannot change qualitatively due to this small asymmetry.

Along with this small off-axis motion, the pWDNS system acquires a small amount of spurious angular momentum. Figure 5 shows the normalized z component of the angular momentum of the system and demonstrates that it is always less than 3% [see Eq. (45)]. In addition to conserving the angular momentum to within 3%, the normalized Hamiltonian constraint violations remain smaller than 1% and the normalized momentum constraint violations smaller than 3%. These results hold for all cases studied in this work.

During the plunge phase the NS penetrates the pWD, launching strong shocks that sweep through and heat the

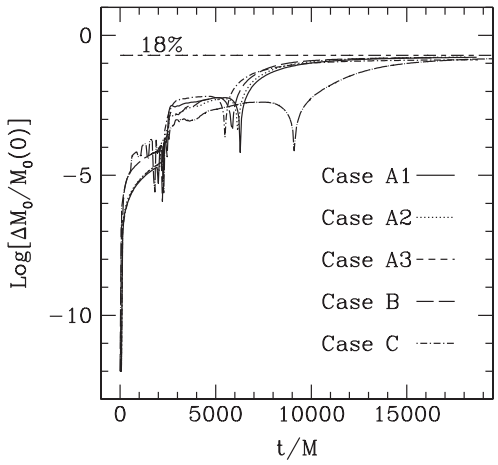

FIG. 7. Fraction of rest mass lost *vs* time. Here $\Delta M_0 = |M_0 - M_0(0)|$, where $M_0(0)$ is the initial total rest mass. Small changes in the rest mass until approximately $5000M$ for cases A1, A2, A3, B and $10\,000M$ for case C are due to interpolations when matter crosses refinement levels and inaccuracies in evolving the very low-density atmosphere. At the end of the simulations the amount of mass ejected is 13.4% of the initial rest mass in case B and ranges from 16.1%–16.7% of the initial rest mass for the other cases. Extrapolating the results to late t we find that in case B $\Delta M_0/M_0(0) \sim 14\%$, $\Delta M_0/M_0(0) \sim 18\%$ in all other cases. Here $M = 2.48 M_\odot = 3.662$ km $= 1.222 \times 10^{-5}$ s.

interior of the pWD. The NS outermost layers are stripped when they encounter the dense central parts of the pWD, and the NS is compressed. We find that at maximum compression in case A2, the NS central density only increases by about 8% of the initial central density.

Eventually, strong shocks sweep through the entire pWD interior and then transfer linear momentum to the pWD outer layers, a large fraction of which receives sufficient momentum to escape to infinity. This can be seen in Fig. 6, where a snapshot is shown of the total energy per unit mass $U = -u_0 - 1$ (subtracting the rest-mass energy) on the equator long after the collision, when ejected material has already started crossing the outer boundary of the computational domain. Unbound ($U > 0$) matter covers most of the computational domain, as shown in Fig. 6. The rest-mass density of the ejected material is of order $10^{-9}\rho_{\rm nuc}$, but the total mass that escapes to infinity is large. This is demonstrated in Fig. 7, which shows the fractional change in the rest mass as a function of time. We find the amount of matter that escapes in cases A1, A2, and A3 is $\simeq 18\%$ of the initial rest mass when we extrapolate our results to late times.

The thermal energy deposited into the ejected material is significant, with $K = P/P_{\rm cold} > 40$. As the ejected matter

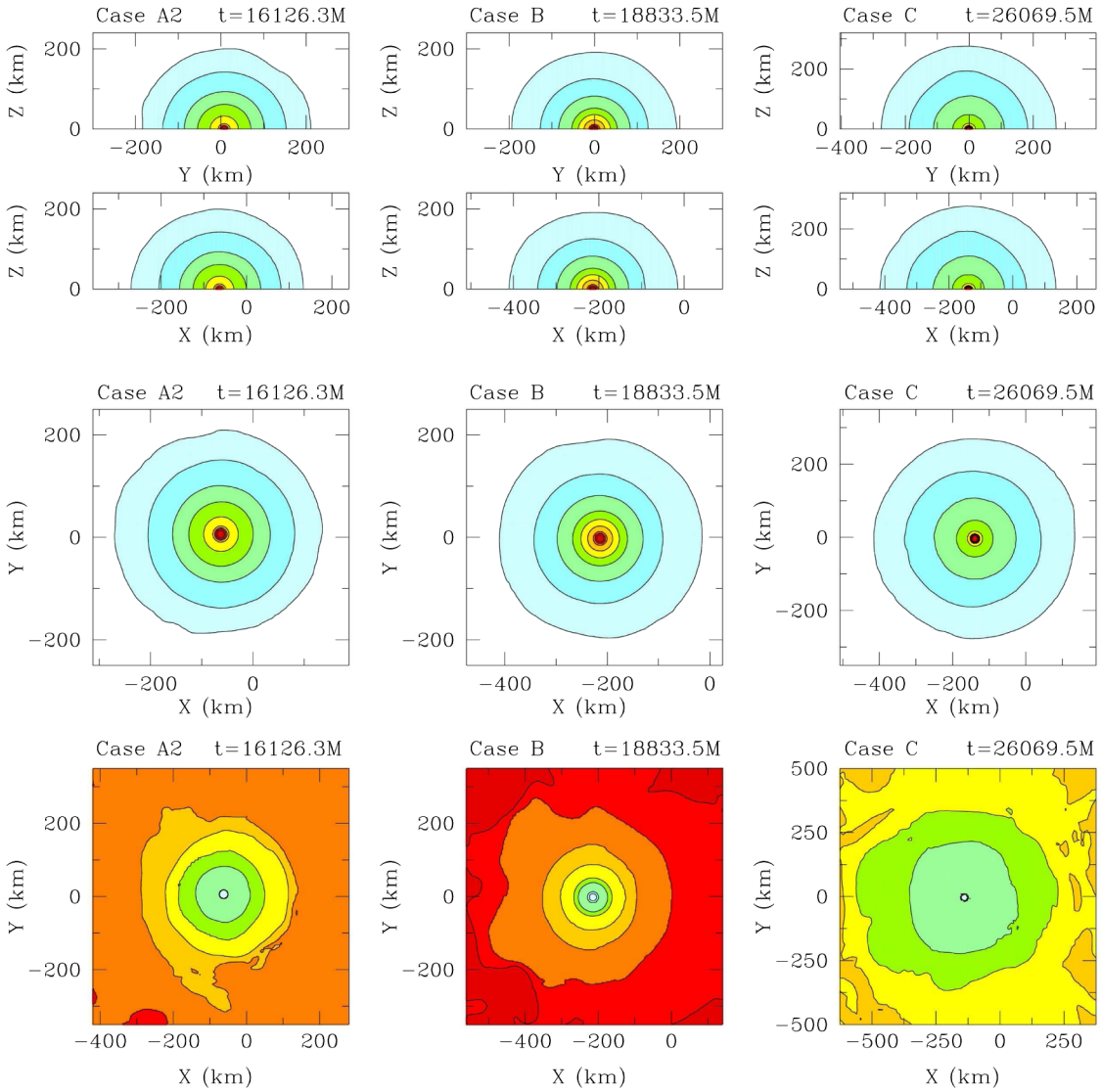

FIG. 8 (color online). First three rows: Snapshots of rest-mass density profiles at the end of the simulation for cases A2, B, C. The contours represent the rest-mass density in the YZ plane (first row), in the XZ plane (second row) and in the XY plane (third row) plotted according to $\rho_0 = \rho_{0,\rm max} 10^{-0.72j-0.16} (j = 0, 1, \ldots, 9)$. The maximum initial NS density is $\rho_{0,\rm max} = 4.6454\rho_{\rm nuc}$. These snapshots demonstrate that in the adopted gauge, the final object is roughly spherical. Last row: Snapshots of $K = P/P_{\rm cold}$ profiles at the end of the simulation for cases A2, B, C. The contours represent K in the XY plane plotted according to $K = 10^{0.288j} (j = 0, 1, \ldots, 9)$. It is evident that the core of the remnant remains cold ($K \simeq 1$). K becomes larger than unity as we move outwards from the center of the objects, and shock heating is more intense in case B and less intense in case C. The color code used is the same as that defined in Fig. 4. Here $M = 2.48 M_\odot = 3.662$ km $= 1.222 \times 10^{-5}$ s.

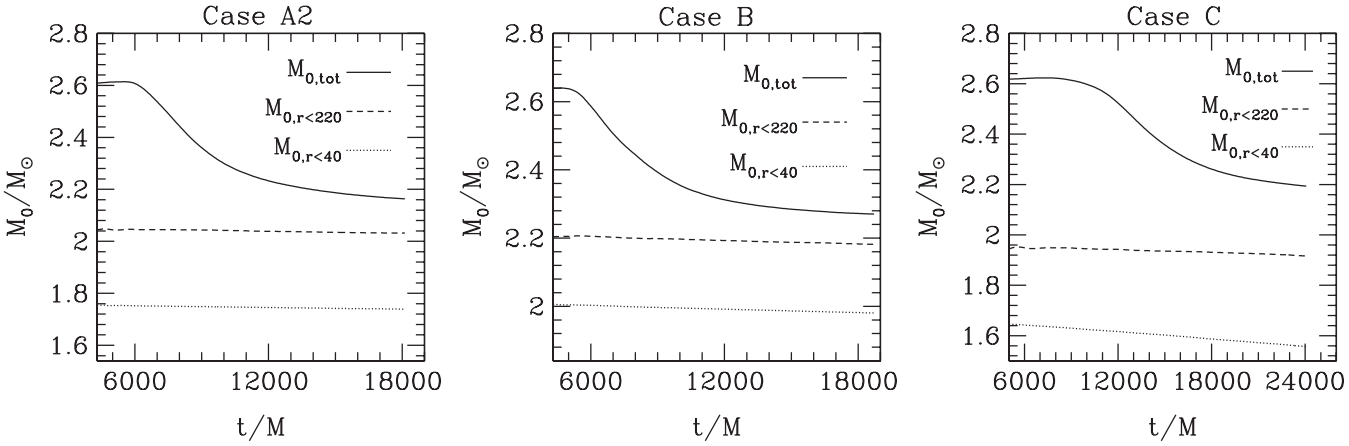

FIG. 9. Post-merger rest mass as a function of time. Here $M_{0,\mathrm{tot}}$ is the total rest mass in the entire computational domain and $M_{0,r<r_0}$ stands for the rest mass contained within a coordinate sphere of radius r_0 in units of km, centered on the remnant's center of mass. In all cases $M_{0,r<220}$ accounts for more than 90% of the final total rest mass and it is always greater than $1.92M_\odot$—the maximum rest mass that our cold EOS can support. Here $M = 2.48M_\odot = 3.662$ km $= 1.222 \times 10^{-5}$ s.

comes from the WD outermost layers, its density is very low. This implies that its initial preshocked sound speed is small. As a result, the Mach number of the ejected material can be very large prior to shock heating, and so shock heating is very strong, i.e., K increases from 1 initially to greater than 40 (see also discussion in Appendix B of [23]).

The time scale for shock heating to equilibrate must be of order few times the dynamical (free-fall) time scale of the WD [see Eq. (2)], as this is the only relevant time scale. For case A, the WD dynamical time scale is roughly 400M. Our computations show that it actually takes about 800M–1000M for the star to equilibrate, which is consistent with the estimate above.

Material that did not receive sufficient thrust to escape to infinity starts to rain down onto the NS and pWD matter and the plunge phase ends when this process is over.

During the quasiequilibrium phase the remnant settles into a spherical quasiequilibrium object whose outer layers oscillate. This can be seen in the two final snapshots of Fig. 4, where we show that the inner equatorial rest-mass density contours do not change with time, while the outer layers change only a little. Figure 8 plots XY, XZ, and YZ rest-mass density contours. Notice that in the adopted gauge, the remnant appears to be spherical.

The pWDNS final remnant consists of a cold NS core with a hot mantle on top. This is demonstrated by the plots in the last row of Fig. 8, where we quantify the results of shock heating by showing contours of $K = P/P_{\mathrm{cold}}$. Within a radius of 100 km from the center of mass of the remnant, K ranges from unity to about 15 for case A2. In all cases $K \simeq 1$ at the center of the remnant, while it becomes larger than unity as we move outwards from the center. We refer to this spherical configuration as a Thorne-Zytkow-like object.

Even though a large fraction of the initial mass escapes, the final total rest mass well exceeds the maximum rest mass of $1.92M_\odot$ our cold EOS can support. In Fig. 9 we show the rest mass of the remnant as a function of time and for various spatial domains. This figure demonstrates that the rest mass within a radius of 220 km accounts for more than 90% of the final total rest mass and is greater than $1.92M_\odot$. However, the pWDNS remnant does not collapse promptly to form a black hole, because of extra support provided by thermal pressure. Delayed collapse to a black hole is almost certain after the pWDNS remnant has cooled.

Finally, we note that it has been suggested in [78,79] that GWs may arise from shocks. Even though the discussion in these studies focused on core collapse supernovae, the appearance of strong shocks in our case can also generate GWs. However, here we do not calculate the GW signature because what is really interesting from an observational and astrophysical point of view is the GW signature in the circular binary WDNS case, not the head-on case we consider. In [33] we did calculate GWs from the inspiral phase of binary WDNS systems. General relativistic computations of the merger of circular binary WDNSs will be the subject of a forthcoming paper.

C. Effects of the pWD compaction

Here we describe the effects of the pWD compaction on the dynamics of pWDNS head-on collisions. Overall, our findings are qualitatively similar to those of case A2 described in the previous section. An appreciable fraction of the initial total mass escapes to infinity, but the final total mass of the pWDNS remnant still exceeds the maximum mass that our cold EOS can support. Prompt collapse to a black hole does not take place either in case B or in case C, because strong shock heating gives rise to a hot remnant. The outcome of cases B and C is again a TZlO.

The three phases of the head-on collision we described in the previous section apply here, too. For this reason we

now focus our discussion on describing the differences between cases B, A2, and C, i.e., in order of decreasing pWD compaction.

The tidal acceleration, which the pWD experiences due to the NS tidal field, increases as the pWD compaction decreases. This is because the initial coordinate separation is the same for cases B, A2, and C. As a result, the acceleration phase is shorter for larger pWD compaction. This can be seen in Figs. 10 and 11, where equatorial rest-mass density contours are plotted.

Shock heating far from the core of the remnants, as quantified by K, is somewhat less intense as the pWD compaction decreases. The shorter acceleration phase implies that the relative speed of the two components at the beginning of the plunge phase is a little smaller, which in turn leads to weaker shocks.

During the plunge phase, the NS interior is less affected by decreasing pWD compaction. This can be seen (a) in the insets in Figs. 10 and 11, where in case C the post-plunge structure of the NS core is almost the same as that showed in the preplunge snapshots, while this is not true for case B, and (b) by the variation in the NS central density ($\rho_{0,c}$); in particular, we find that at maximum compression the NS central density increases by about 42% in case B, 8% in case A2 and 5% in case C. These results can be easily interpreted because in a sequence of pWDNS head-on collisions where the NS is fixed and the size of the pWD increases with fixed mass, the NS gradually encounters thinner and thinner material, and hence changes to the NS structure become less and less important.

Were the system mass loss to vary appreciably with pWD size, we might expect a corresponding variation in $\rho_{0,c}$. However, such a mass loss variation is not observed, as we discuss next.

As in case A2, in both cases B and C, a large fraction of the initial mass eventually escapes to infinity (see Fig. 6 for case B), but we do not find strong variations in the mass lost among cases B, A2, and C. We find that the amount of matter that escapes in case B is 14% of the initial rest mass, while case C loses 18%, (case A2 loses 18%) [see Fig. 7] of the initial rest mass. Given our earlier discussion that shocks in case B are stronger than those in case A2, and in turn shocks in case A2 are stronger than those in case C, this last result may sound contradictory, because one might expect that stronger shocks would eject more matter to infinity. The apparent contradiction can be resolved, if one considers that as the pWD compaction decreases, the pWD outer layers become less and less bound, and hence, it requires less energy to eject them to infinity.

As in case A2, the remnants in cases B and C eventually settle into spherical quasiequilibrium objects with oscillating outer layers (see Figs. 10 and 11). The sphericity of the

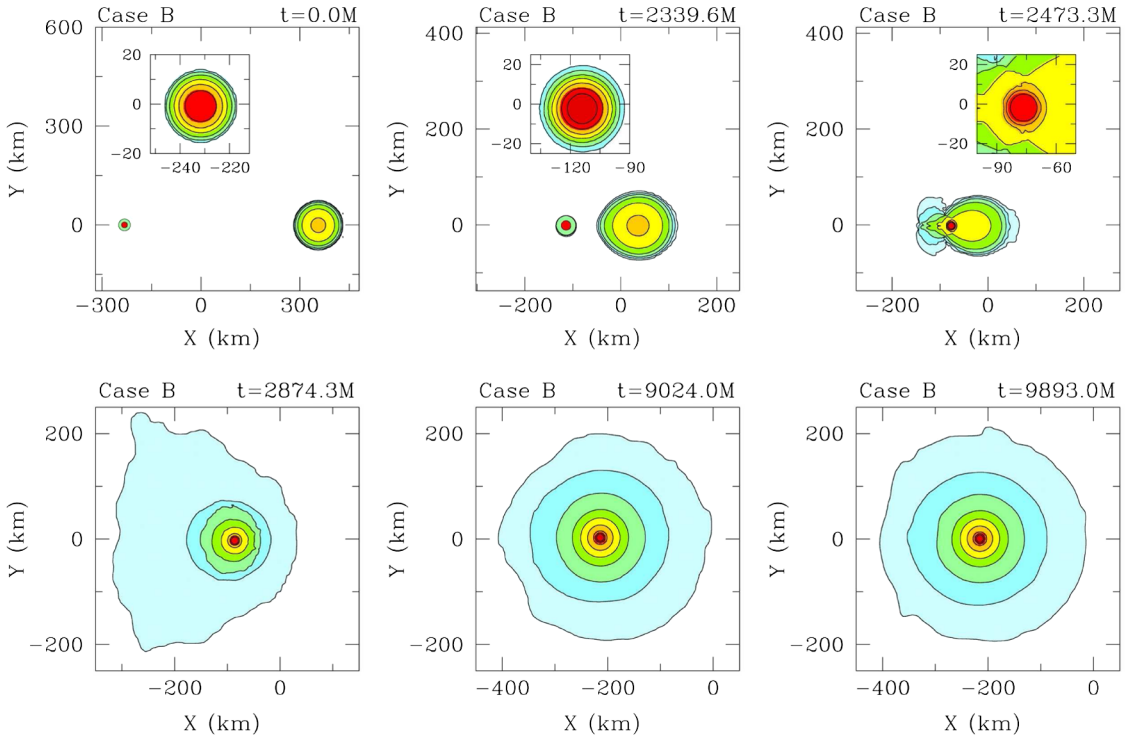

FIG. 10 (color online). Snapshots of rest-mass density contours at selected times for case B. The contours are plotted in the orbital plane, according to $\rho_0 = \rho_{0,\max} 10^{-0.61j-0.16} (j = 0, 1, \ldots, 9)$. The color code used is the same as that defined in Fig. 4. The maximum initial NS density is $\rho_{0,\max} = 4.6454 \rho_{\rm nuc}$. The last two snapshots, which take place near the end of the simulation, demonstrate that the density contours within a radius of about 150 km remain unchanged. Here $M = 2.48 M_\odot = 3.662$ km $= 1.222 \times 10^{-5}$ s is the sum of the isolated stars' ADM masses.

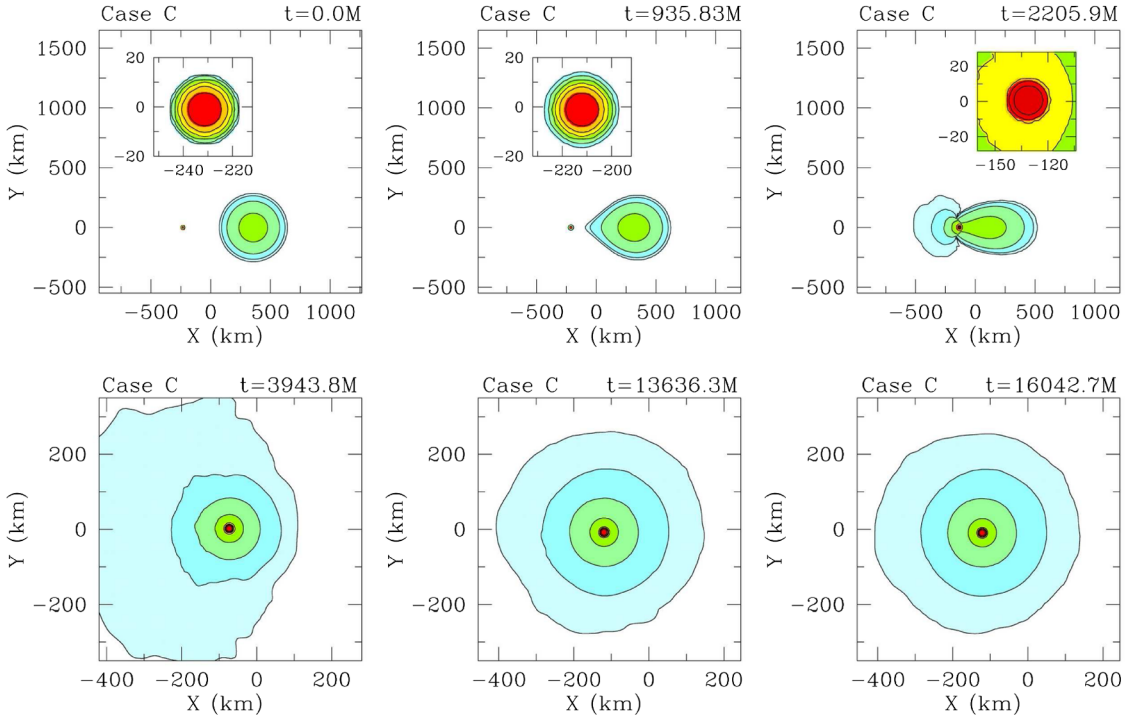

FIG. 11 (color online). Rest-mass density contours in the orbital plane at selected times for case C. The contours are plotted according to $\rho_0 = \rho_{0,\max} 10^{-0.72j-0.16} (j = 0, 1, \ldots, 9)$. The color code used is the same as that defined in Fig. 4. The maximum initial NS density is $\rho_{0,\max} = 4.6454\rho_{\rm nuc}$. The last two snapshots, which take place near the end of the simulation, demonstrate that the density contours within a radius of about 150 km remain unchanged. Here $M = 2.48M_\odot = 3.662$ km $= 1.222 \times 10^{-5}$ s is the sum of the isolated stars' ADM masses.

remnants (in the adopted gauge) in cases B and C is demonstrated by the XY, XZ, and YZ rest-mass density contours shown in Fig. 8.

The pWDNS remnants in both case B and case C consist of a cold NS core with a hot mantle on top. Thus, all cases lead to the formation of a TZlO. This is again demonstrated in the last row of Fig. 8, where contours of $K = P/P_{\rm cold}$ are shown. Within a radius of about 100 km from the center of mass of the final remnants, $K \in [1, 35]$ in case B, and $K \in [1, 10]$ in case C ($K \in [1, 15]$ in case A2). Thus, shock heating is overall strongest in case B, weaker in case A2 and even weaker in case C.

In Fig. 9 the remnant rest masses in cases B and C are plotted as functions of time. The figure demonstrates that in both cases, the rest masses within a radius of 220 km account for more than 90% of the final total rest masses in both case B and case C, and are greater than $1.92M_\odot$, i.e., the maximum rest mass that our cold EOS can support. The pWDNS remnant does not collapse promptly to form a black hole, because of the extra thermal pressure support. However, delayed collapse to a black hole is almost certain after the pWDNS remnant has cooled.

Another important feature of Fig. 9 is that the amount of mass contained within a given radius from the center of mass of the remnant is larger for smaller initial pWDs. For example, within a radius of 220 km the remnant mass is $2.18M_\odot$ in case B, $2.035M_\odot$ in case A2, and $1.90M_\odot$ in case C. This in turn indicates that the higher the initial pWD compaction the higher the core densities of the pWDNS remnant. This is supported by the rest-mass density contours shown in Fig. 8 and by the values of the final central rest-mass density. In particular, we find that the final central rest-mass density is $4.10\rho_{\rm nuc}$ in case C, $4.49\rho_{\rm nuc}$ in case A2, and $4.91\rho_{\rm nuc}$ in case B. Thus, there is a variation in the final central density of 9.2% from case B to case A2, and 9.5% from case A2 to case C. Finally, it is also worth noting that the final minimum value of the lapse function, which is a good indicator of collapse, increases with increasing initial pWD size, too. Specifically, we find this value to be 0.57 in case B, 0.595 in case A2, and 0.609 in case C. All these facts seem to indicate that as the pWD size increases towards realistic WD sizes the less likely it is for the pWDNS remnant to collapse. To demonstrate this trend more clearly we compile all aforementioned physical parameters of the final configurations in cases B, A2, and C in Table IV.

Hence, given the consistency in the results of cases B, A2, and C, i.e., the sequence of increasing pWD size with fixed pWD mass, we expect that as the parameters of our EOS vary, so as to describe realistic WDs, the result of the head-on collision of a massive WDNS system will most likely lead to formation of a quasiequilibrium TZlO. If the initial total mass of the system exceeds the maximum mass

TABLE IV. Summary of pWD compaction study. Here $C_{\rm WD}$ is the compaction of an isolated pWD (see Table II), $K = P/P_{\rm cold}$ at the end of simulations[a], T_p is the peak temperature at the end of simulations, $M_0(0)$ is the initial total rest mass, $\Delta M_0 = |M_{0,f} - M_0(0)|$, where $M_{0,f}$ is the final total rest mass, $M_{0,r<220}$ is the mass enclosed within 220 km from the center of mass of the remnant at the end of the simulations, $\rho_{0,c}$ is the final value of the central rest-mass density [b], and $\alpha_{\rm min}$ the final value of the minimum of the lapse function.

Case	$C_{\rm WD}$	K	$T_p(10^{11}\ ^o{\rm K})$[c]	$\Delta M_0/M_0(0)$	$M_{0,r<220}/M_\odot$	$\rho_{0,c}/\rho_{\rm nuc}$	$\alpha_{\rm min}$
B	0.0190	[1,35]	3.7	14%	2.180	4.91	0.570
A2	0.0100	[1,15]	3.2	18%	2.035	4.49	0.595
C	0.0049	[1,10]	3.0	18%	1.900	4.10	0.609

[a]The K column lists the range of values which K obtains within a radius of 100 km from the centers of mass of the remnants.
[b]$\rho_{\rm nuc} = 2 \times 1014$ g/cm^3.
[c]For realistic WDNS collisions we expect $T_p \sim 10^9\ ^o$K [see discussion following Eq. (51)].

a cold EOS can support, then the TZlO may have mass that exceeds the maximum mass a cold EOS can support, so it will eventually undergo collapse to a black hole, but only after the remnant has cooled.

To identify the dominant cooling mechanisms and/or relevant nuclear reaction networks, one would need to estimate the temperatures of these TZlOs. We can do this as follows.

Using Eq. (40) and the definition of K we can calculate the specific thermal energy as

$$\epsilon_{\rm th} = \frac{(K-1)P_{\rm cold}}{(\Gamma_{th}-1)\rho_0}. \tag{48}$$

To estimate the temperature T of matter, we assume that we can model the temperature dependence of $\epsilon_{\rm th}$ as

$$\epsilon_{\rm th} = \frac{3kT}{2m_n} + f\frac{aT^4}{\rho_0}, \tag{49}$$

where m_n is the mass of a nucleon, k is the Boltzmann constant and a is the radiation constant. The first term represents the approximate thermal energy of the nucleons, and the second term accounts for the thermal energy due to relativistic particles. The factor f reflects the number of species of ultrarelativistic particles that contribute to the thermal energy. When $T \ll 2m_e/k \sim 10^{10}$ K, where m_e is the electron mass, thermal radiation is dominated by photons and $f = 1$. When $T \gg 2m_e/k$, electrons and positrons become ultrarelativistic and also contribute to radiation, and $f = 1 + 2 \times (7/8) = 11/4$. At sufficiently high temperatures and densities ($T \geq 10^{11}$ K, $\rho_0 \geq 10^{12}$ g cm^{-3}), neutrinos are generated copiously and become trapped, so, taking into account three flavors of neutrinos and antineutrinos, $f = 11/4 + 6 \times (7/8) = 8$.

In Fig. 12 we show the temperature profiles of the remnants in cases B, A2, and C, where it is clear that typical temperatures of our TZlOs are of order $10^{11}\ ^o$K. This is expected as the total energy available for shock heating should be of order $M_{\rm NS}M_{\rm WD}/R_{\rm WD}$, i.e., the gravitational interaction energy when the two stars first make contact. The total thermal energy, $E_{\rm th}$, is then

$$E_{\rm th} \sim \frac{(M_{\rm NS} + M_{\rm WD})}{m_n} kT \sim \frac{M_{\rm NS}M_{\rm WD}}{R_{\rm WD}}. \tag{50}$$

From this last equation we can estimate the characteristic temperature as

$$T \sim \frac{C_{\rm WD}m_n}{(1+q)k}. \tag{51}$$

Thus, all things being equal (no mass loss, same kinetic energy at collision, etc.) characteristic TZlO temperatures should be directly proportional to the pWD compaction. Taking case A2 as an example, $C \simeq 0.01$ and $q \simeq 2/3$, we find $T \simeq 6.5 \times 10^{10}\ ^o$K, in rough agreement with our simulations.

Using this scaling argument we can extrapolate our results to realistic WDNS head-on collisions. For a solar-mass WD obeying the Chandrasekhar EOS $C_{\rm WD} \simeq 3 \times 10^{-4}$. Hence, we predict that typical temperatures in

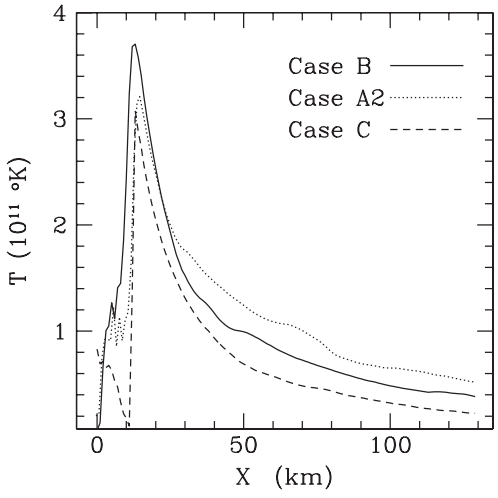

FIG. 12. Temperature (T) profiles for cases B, A2, and C. The temperature is in units of $10^{11}\ ^o$K. The profiles correspond to the values of T at the end of the simulations and along the x-axis (for $x > x_c$, where x_c is the x position of the center of mass of the remnant in each case). It is clear that typical temperatures are of order $10^{11}\ ^o$K. For realistic WDNS collisions we expect $T \sim 10^9\ ^o$K [see discussion following Eq. (51)].

realistic head-on collisions of massive WDNS systems would be of order 10^9 ^{o}K.

VII. SUMMARY AND DISCUSSION

In this work we studied the dynamics of the head-on collision of WDNS binaries in full general relativity, aided by simulations that employ the Illinois AMR relativistic hydrodynamics code [23,58]. This study serves as a prelude to the circular binary WDNS problem which will be the subject of a forthcoming paper.

Our primary focus is on compact objects whose total mass exceeds the maximum mass that a cold EOS can support and our goal is to determine whether a WDNS collision leads either to prompt collapse to a black hole or the formation of a quasiequilibrium configuration that resembles a TZO [57], which we call TZlO. By a TZlO we mean a NS sitting at the center of a hot gaseous mantle composed of WD debris.

Because of the vast range of dynamical time scales and length scales involved in this problem, realistic WDNS simulations (head-on or otherwise) are computationally prohibitive, if one employs current numerical relativity techniques and available computational resources. For this reason, we tackle the problem using a different approach.

In particular, we constructed a piecewise polytropic EOS which captures the main physical features of NSs and, at the same time, scales down the size of a WD. We call these scaled-down models of WDs pseudo-WDs. Using these pWDs, we can reduce the range of length scales and time scales involved, rendering the computations feasible.

A pWD is not a realistic model of a WD. However, with our proposed parametrized EOS we can construct a sequence of pWD models with gradually increasing size and perform simulations that approach the realistic case. Then we can make predictions about the realistic case by extrapolating the results from this sequence of simulations.

Using pWDs, we performed two sets of simulations. One set of our simulations studied the effects of the NS mass on the final outcome, when the pWD is kept fixed at a mass of $0.98M_\odot$ and its size fixed at 146 km. We choose three masses for the NS, namely $1.4M_\odot$, $1.5M_\odot$, $1.6M_\odot$ (cases A1, A2, and A3, respectively). The other set of simulations studied the effect of the pWD compaction on the final outcome, when the NS is kept fixed at a mass of $1.5M_\odot$. In the latter set of calculations, we choose three values for the ratio of the pWD to the NS radius, namely, 5:1, 10:1 and 20:1 (cases B, A2, and C, respectively).

In general, the head-on collision of pWDNS systems can be decomposed in three phases: (i) acceleration, (ii) plunge and (iii) quasiequilibrium.

During the acceleration phase the two stars accelerate towards one another starting from rest. As the separation decreases the NS tidal field becomes so strong that the pWD becomes highly distorted, while the NS interior is almost unchanged. This phase ends when the NS and pWD first make contact.

During the plunge phase the NS penetrates the pWD, launching strong shocks that sweep through and heat the interior of the pWD. The NS outermost layers are stripped after encountering the dense central parts of the pWD (see Fig. 4), but the NS core is mostly unaffected, except when the compaction of the pWD is high (see Sec. VI C). We find that the strong shocks sweeping the pWD transfer linear momentum to the outer pWD layers, causing a large amount of pWD matter to escape to infinity. In all calculations, we find the rest mass loss to be between 14%–18% of the initial total rest mass. Material that did not escape to infinity accretes onto the underlying NS and pWD matter.

Finally, during the quasiequilibrium phase, the remnant settles into a spherical quasiequilibrium object whose outermost layers undergo damped oscillations.

Although a large fraction of the initial mass escapes, the final total rest mass still exceeds the maximum rest mass of $1.92M_\odot$ that our cold EOS can support (see Fig. 9). However, the pWDNS remnant cannot collapse promptly to form a black hole, because it is hot. This result is the same in all our simulations. However, we point out that delayed collapse to a black hole is almost certain after the pWDNS remnant has cooled, but this will occur on a time scale much larger than a hydrodynamical time scale.

The final object consists of a cold NS core surrounded by a hot mantle. We quantified the results of shock heating by the ratio of the total pressure to the cold pressure $K = P/P_{\rm cold}$. In all cases $K \simeq 1$ at the center of the remnant, and becomes larger than unity away from the center. We refer to this nearly-spherical configuration as a Thorne-Zytkow-like object, and find this object at the end of all simulations, regardless of NS mass and pWD compaction. We find that within a radius of 100 km from the centers of mass of the remnants, K lies in the range [1, 15] in cases A1, A2, and A3, [1, 35] in case B and [1, 10] in case C. Using a simple model for the temperature dependence of the specific thermal energy we estimate the characteristic temperature of these objects to be of order 10^{11}^{o}K. Using a simple scaling argument [see Eq. (51)] we find that TZlO temperatures should be proportional to the compaction of the original pWD, so that in realistic WDNS head-on collisions typical remnant temperatures would be of order 10^9 ^{o}K.

Furthermore, we find that the smaller the initial pWD compaction the smaller the core densities of the pWDNS remnant. This is supported by the rest-mass density contours shown in Fig. 8 and by the values of the final central rest-mass density. In particular, we find that the final central rest-mass density decreases by 9.2% from case B to case A2, and 9.5% from case A2 to case C. In addition, the final minimum value of the lapse function, which is a good indicator of collapse, increases with increasing initial pWD size, too. Specifically, we find this value to be 0.57 in

case B, 0.595 in case A2, and 0.609 in case C (see Table IV for a summary of physical parameters of the final configurations in cases B, A2, C). All these facts seem to indicate that as the pWD size increases towards realistic WD sizes the less likely it is for the pWDNS remnant to collapse.

An important concern regards the invariance of these results with respect to larger initial separations. To fully resolve this, one would need to extend the simulations to wider separations, but this extension is outside the scope of the current work. However, this work gives us some qualitative idea about what might happen with larger initial separations. Larger separations imply larger kinetic energies during the plunge phase, which in turn imply stronger shocks. Stronger shocks likely lead to larger mass loss and more intense shock heating. Therefore, our expectation is that head-on collisions of pWDNS systems starting at larger separations will also result in the formation of TZlOs and that such collisions would not lead to prompt formation of a black hole.

Given the consistency in the results of cases B, A2, and C, we expect that as the parameters of our EOS are adjusted such that pWDs more closely resemble realistic WDs, WDNS head-on collisions are likely to form a quasiequilibrium TZlO. If the initial total mass of the system well exceeds the maximum mass that a cold EOS can support, then the TZlO will most likely have mass exceeding the maximum mass supportable by a cold EOS, eventually collapsing to a black hole after the remnant has cooled.

We conclude by stressing that we cannot use the results of this work to make definite predictions about either the pWDNS or the realistic WDNS circular binary problem. One might speculate that shock heating will be minimized in such a scenario, and hence it may result in prompt collapse to a black hole. However, sufficient angular momentum must be shed in the circular binary case in order for the object to promptly form a black hole. To resolve these issues, hydrodynamic simulations in full general relativity must be performed and will be the focus of a forthcoming paper.

ACKNOWLEDGMENTS

We would like to thank A. M. Khokhlov and T. W. Baumgarte for helpful discussions. This paper was supported in part by NSF Grant Nos. PHY06-50377 and PHY09-63136 as well as NASA Grant Nos. NNX07AG96G and NNX10AI73G to the University of Illinois at Urbana-Champaign. Z. Etienne gratefully acknowledges support from the NSF.

APPENDIX A: INITIAL DATA CODE DESCRIPTION

In this appendix we describe some details of the FMR, finite difference code we developed for generating general relativistic initial data.

The grid structure we use is a multilevel set of properly nested, cell-centered uniform grids. Each grid corresponds to one level of refinement labeled by the level number $il = (0, 1, 2, \ldots, nl - 1)$, where nl is the total number of levels. $il = 0$ corresponds to the coarsest level and $il = nl - 1$ to the finest one. All levels have the same number of grid points $nx, ny, nz \in \mathbb{Z}$ in the x, y and z directions, respectively. The coordinates on our grid are defined as follows:

$$\begin{aligned} x_{il,i} &= x_{il,\min} + i \cdot \Delta x_{il}, \quad i = 0, 1, \ldots, nx - 1, \\ y_{il,j} &= y_{il,\min} + j \cdot \Delta y_{il}, \quad j = 0, 1, \ldots, ny - 1, \\ z_{il,k} &= z_{il,\min} + k \cdot \Delta z_{il}, \quad k = 0, 1, \ldots, nz - 1, \end{aligned} \tag{A1}$$

where $x_{il,\min}$, $y_{il,\min}$, $z_{il,\min}$ are the minimum values of the coordinates in each direction on level il and Δx_{il}, Δy_{il}, Δz_{il} are the mesh sizes in each direction on level il.

The mesh size between two consecutive levels differs by a factor of 2 so that

$$\Delta x_{il+1} = \frac{\Delta x_{il}}{2}, \tag{A2}$$

and similarly in the y and z directions.

In order for the grids to be properly nested we demand that there exists an $i \in [0, nx - 1]$ such that

$$x_{il,i} = x_{il+1,\min} - \frac{3}{2}\Delta x_{il+1}, \quad il = 0, \ldots nl - 2 \tag{A3}$$

and similarly in the y and z directions. This condition ensures that two consecutive levels share a common interface.

We now borrow FMR terminology to name two types of cells that exist on our grid. These are the split cells and the leaf cells or leaves. A split cell is one within which there exist higher level cells and a leaf cell is one within which there are no higher level cells. The total number of cells N_{tot} on our grid is

$$N_{\text{tot}} = nx \cdot ny \cdot nz \cdot nl, \tag{A4}$$

and a straightforward calculation shows that the number of leaves is

$$N_{\text{leaf}} = nx \cdot ny \cdot nz \frac{7nl + 1}{8}. \tag{A5}$$

When $nl = 1$, $N_{\text{leaf}} = N_{\text{tot}}$, i.e., all cells are leaves, as expected.

We distinguish between these two types of cells because our solutions are defined only on leaves. This may be more cumbersome to implement, but has two main advantages.

First, there is no ambiguity as to how one should interpolate values of matter sources from fine levels on coarse levels in order to correctly calculate the gravitational fields. To be more specific, let us assume that we have one coarse cell which is split into 8 cells and that we know the values of the density on the fine cells. In Newtonian physics, to ensure that the gravitational fields are computed correctly

(at least far away), all we have to do is set the cell averaged density on the coarse level such that the total mass in the coarse cell is the same as the total mass in the enclosed fine cells. In general relativity the definition of gravitational mass depends not only on the density, but also on the gravitational fields. Hence, there is no straightforward way to set the density on coarse cells in GR. The ambiguity is immediately lifted, if one defines all fields only on the finest cells.

The second advantage of using only leaves is that the memory requirements are minimized and the calculations are carried out faster because

$$\frac{N_{\rm leaf}}{N_{\rm tot}} = \frac{7nl+1}{8nl} \leq 1, \tag{A6}$$

where the last inequality holds because $nl \geq 1$.

For a general second-order nonlinear elliptic equation of the form

$$\nabla^2 u = f(u)\chi, \tag{A7}$$

where $f(u)$ is a nonlinear function of the variable u and χ a known scalar independent of u, our code employs a standard second-order finite difference scheme

$$\begin{aligned}&\frac{u_{il,i+1,j,k} + u_{il,i-1,j,k} - 2u_{il,i,j,k}}{\Delta x_{il}^2} \\ &+ \frac{u_{il,i,j+1,k} + u_{il,i,j-1,k} - 2u_{il,i,j,k}}{\Delta y_{il}^2} \\ &+ \frac{u_{il,i,j,k+1} + u_{il,i,j,k-1} - 2u_{il,i,j,k}}{\Delta z_{il}^2} \\ &= f(u_{il,i,j,k})\chi_{il,i,j,k}.\end{aligned} \tag{A8}$$

The finite difference stencil changes only across grid-level boundaries where we perform first-order interpolation.

To address the nonlinearity of Eq. (A7) we perform Newton-Raphson iterations as follows. Let us assume that u_n is a guess at step n. We first calculate the residual R_n from Eq. (A7)

$$R_n = \nabla^2 u_n - f(u_n)\chi, \tag{A9}$$

and then solve the linearized equation for the correction δu_n on u_n

$$\nabla^2 \delta u_n = f'(u_n)\chi\delta u_n - R_n, \tag{A10}$$

where

$$f'(u_n) = \left(\frac{df(u)}{du}\right)_{u=u_n}. \tag{A11}$$

Once a solution to (A10) is found, we correct u_n as

$$u_{n+1} = u_n + \delta u_n, \tag{A12}$$

and iterate until this procedure converges and a solution to Eq. (A7) is obtained.

We solve the equations using the PETSc linear solver Krylov space methods. Krylov space methods are matrix methods and hence we have to set up the matrix of the linear system.

To do this we define a global index that counts all cells (both leaves and split cells) on our grid as

$$I = il + nl(i + nx \cdot j + nx \cdot ny \cdot k), \tag{A13}$$

In this way, every leaf cell corresponds to a unique index I. However, I takes values $0, 1, \ldots, N_{\rm tot} - 1$, but there are $N_{\rm leaf}$ leaves on the grid with $N_{\rm leaf} \leq N_{\rm tot}$. Hence I cannot be used to count leaves, unless $nl = 1$. For this reason, we define another index ic, which counts only the leaves on our grid, as well as two mappings; from I to ic, $ic(I)$ and from ic to I, $I(ic)$. Since for every cell on our grid we can find I from Eq. (A13) we set up these mappings by defining two arrays ic_of_I, I_of_ic, of length $N_{\rm tot}$ and $N_{\rm leaf}$, respectively. Looping over il, i, j, k, we store ic in the array ic_of_I assigning a value of -1 for split cells, whereas we store I in the array I_of_ic. The index I is used when we need the index ic of a neighbor leaf cell in order to calculate derivatives or enter matrix elements.

For example, let us assume that we are at a leaf cell of index ic which is not near a grid-level boundary, and we want to enter the element of matrix A that corresponds to the right-x neighbor of this cell (where A represents the Laplacian). From Eq. (A8) this matrix element must be $1/\Delta x_{il}^2$. If ic represents the ic-th row of A we must find which column of A the neighbor corresponds to. We find this as follows.

First, using the mapping from ic to I, we find the index $I = I(ic)$ of the leaf. Next by use of Eq. (A13) we determine il, i, j, k that correspond to I using the following sequence of operations

$$\begin{aligned}k &= \text{int}(I/nl \cdot nx \cdot ny), \\ I_1 &= I - nl \cdot nx \cdot ny \cdot k, \\ j &= \text{int}(I_1/nl \cdot nx), \\ I_2 &= I_1 - nl \cdot nx \cdot j, \\ i &= \text{int}(I_2/nl \cdot nx), \\ il &= I_2 - nl \cdot i,\end{aligned} \tag{A14}$$

where int means the integer part of the division.

In the next step the global index (I_{p1}) of the right x-neighbor is found, as $I_{p1} = il + nl(i + 1 + nx \cdot j + nx \cdot ny \cdot k)$. Finally, using the mapping from I to ic we find the leaf (or desired column) number $ic_{p1} = ic(I_{p1})$. Knowing the column number of the neighbor, it is straightforward to assign $A_{ic,ic_{p1}} = 1/\Delta x_{il}^2$. We use the same approach to set up all the matrix elements of the linear systems and calculate derivatives. The algorithm becomes slightly more complicated when the neighbor cell is a fictitious cell that resides on a different level. In such cases we perform first-order interpolation and use the same

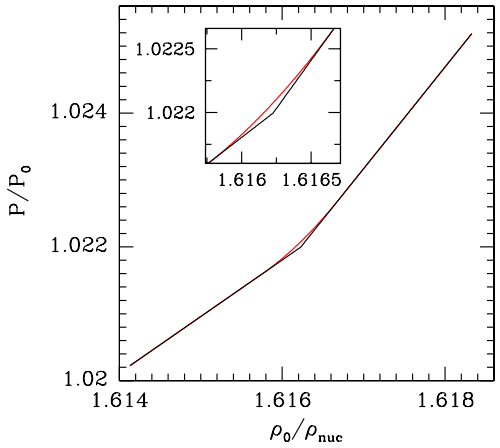

FIG. 13 (color online). Pressure vs rest-mass density for EOSs (B1) [black or thick curve in gray scale] and (B2) [red or thin curve in gray scale]. Here $P_0 = 10^{-5}$ km^{-2} and $\rho_{\rm nuc} = 1.48494 \times 10^{-4}$ km^{-2}. The inset zooms in the region, where EOS (B1) is nondifferentiable, and shows that the cubic spline fit smooths out the discontinuity.

method as outlined above to find which matrix elements must be filled with nonzero values.

APPENDIX B: VALIDATION OF THE HIGH-RESOLUTION SHOCK-CAPTURING METHOD FOR A PIECEWISE POLYTROPIC EOS

In this appendix we analyze the effect our numerical schemes have on solutions obtained with our adopted nonsmooth EOS (15) and a smooth counterpart of this EOS. We show that there is no essential difference. This result is expected because an algorithm with finite resolution cannot distinguish a smooth EOS from a nonsmooth EOS, if the smoothing operation is performed below the resolution level of the computations.

For simplicity we consider a nonsmooth EOS with two branches as follows

$$P = \begin{cases} \kappa_1 \rho_0^{1+1/n_1}, & \rho_0 \le \rho_1 \\ \kappa_2 \rho_0^{1+1/n_2}, & \rho_0 > \rho_1, \end{cases} \tag{B1}$$

and perform a smoothing operation over a density interval $[\rho_i(1-\epsilon), \rho_i(1+\epsilon)]$ as follows:

$$P = \begin{cases} \kappa_1 \rho_0^{1+1/n_1}, & \rho_0 \le \rho_1(1-\epsilon) \\ f(\rho_0), & \rho_1(1-\epsilon) < \rho_0 \le \rho_1(1+\epsilon), \\ \kappa_2 \rho_0^{1+1/n_2}, & \rho_0 > \rho_1(1+\epsilon), \end{cases} \tag{B2}$$

where $f(\rho_0)$ is a smooth spline fit such that the EOS is continuous and has continuous first or second derivative, depending on the order of the spline. Our particular choice for the smoothing function is either a cubic spline or a quintic spline. In the former case the EOS becomes C^1, while in the latter case the EOS becomes C^2.

We chose ϵ to be sufficiently small so that the smoothed EOS mimics as closely as possible EOS (B1), but large enough to avoid round off errors due to very large gradients. For the cubic spline we set $\epsilon = 10^{-4}$, while for the quintic spline we set $\epsilon = 10^{-2}$. In all our numerical tests we choose k_1, k_2, n_1, n_2, ρ_1 to correspond to k_2, k_3, n_2, n_3, ρ_2 of the 10:1 EOS (see Table I), respectively. In Fig. 13 we show a plot of EOSs (B1) and (B2), where $f(\rho_0)$ is a cubic spline.

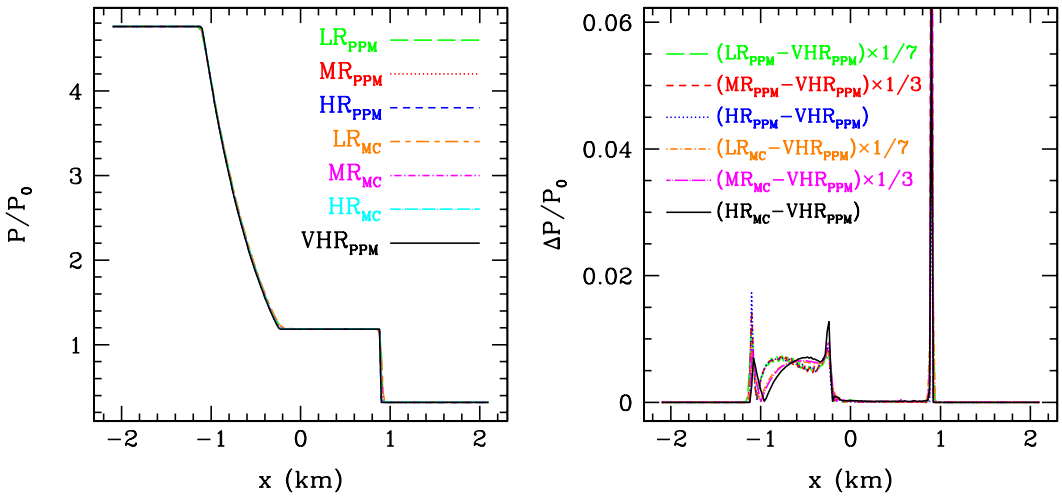

FIG. 14 (color online). Left: Snapshot of pressure profile at $t = 2.56$ km, corresponding to a third of a sound speed crossing time scale across the domain. Right: Convergence plot (at $t = 2.56$ km) using as reference solution the very high-resolution solution obtained in conjunction with the smooth EOS (B2) with a cubic spline smoothing function. The labels in the plots denote the resolution (LR, MR, HR, or VHR) and the reconstruction method (PPM or MC as subscripts). The resolutions used are: LR = 210, MR = 420, HR = 840, VHR = 1680 grid points. PPM stands for the piecewise parabolic reconstruction, and MC stands for the monotonized central reconstruction. The plots demonstrate that all solutions overlap (left panel), regardless of the reconstruction method and the EOS used (smooth or nonsmooth), and first-order convergence to the VHR run with the smooth EOS, as expected. Here $P_0 = 10^{-5}$ km^{-2}.

With the smooth EOS (B2) at our disposal we set up several 1D Riemann (or shock tube) problems in a spatial domain of length $L = 4.2$ km and resolutions 210, 420, 840 and 1680 grid points. We set $\Gamma_{\rm th} = 1.66$ and use Eq. (40) with $P_{\rm cold}$ given by either EOS (B1) or EOS (B2).

We have explored the parameter space of initial data (ρ_L, P_L, u^x_L), (ρ_R, P_R, u^x_R) for the left and right states, and in all cases we found that the solutions obtained with EOS (B1) almost overlap those obtained with the smooth EOS (B2). These results hold for both PPM and monotonized central (MC) reconstruction, regardless of resolution and the spline fit choice. Furthermore, we verified that all our simulations with the smooth EOS (B2) had high enough resolution so that data points would sample the smoothing interval $[\rho_i(1-\epsilon), \rho_i(1+\epsilon)]$ every few time steps.

In Fig. 14 we plot a snapshot of the pressure profile and do a convergence test for one of the cases we simulated with $(\rho_R = 10^{-4},\ P_R = P_{\rm cold}(\rho_R),\ u^x_R = 0)$, $(\rho_L = 5 \times 10^{-4},\ P_L = 10 P_R,\ u^x_L = 0)$. The figure shows that all solutions overlap (left panel) and converge at the expected order (right panel) to the very high-resolution solution obtained with PPM in conjunction with the smooth EOS.

The solutions obtained with the smooth EOS (B2) with quintic spline smoothing, which results in a C^2 and a convex EOS, also overlap with those of the nonsmooth EOS solutions even though the smoothing interval we chose was much larger than in the cubic spline case, and hence the data points would sample it more frequently. Note also that the coarsest resolution used in the shock tube tests is at least 20 times higher than the resolution used in our WDNS simulations. Therefore, all these results demonstrate that our numerical methods capture the correct solution and indicate that no unphysical solutions are present in our simulations of the WDNS head-on collisions.

[1] B. Abbott *et al.* (LIGO Scientific Collaboration), Phys. Rev. D **77**, 062002 (2008).
[2] D. A. Brown *et al.*, Classical Quantum Gravity **21**, S1625 (2004).
[3] F. Acernese *et al.* (VIRGO Collaboration), Classical Quantum Gravity **23**, S635 (2006).
[4] F. Bauville *et al.*(LIGO-VIRGO Working Group), Classical Quantum Gravity **25**, 045001 (2008).
[5] H. Lück *et al.* (GEO600 Collaboration), Classical Quantum Gravity **23**, S71 (2006).
[6] M. Ando *et al.* (TAMA Collaboration), Classical Quantum Gravity **19**, 1409 (2002).
[7] D. Tatsumi *et al.* (TAMA Collaboration), Classical Quantum Gravity **24**, S399 (2007).
[8] http://www.gravity.uwa.edu.au/docs/aigo_prospectus.pdf.
[9] G. Heinzel, C. Braxmaier, K. Danzmann, P. Gath, J. Hough, O. Jennrich, U. Johann, A. Rüdiger, M. Salusti, and H. Schulte, Classical Quantum Gravity **23**, S119 (2006).
[10] S. Kawamura *et al.* (DECIGO Collaboration), Classical Quantum Gravity **23**, S125 (2006).
[11] T. W. L. Baumgarte and S. L. Shapiro, *Numerical Relativity* (Cambridge University Press, Cambridge, England, 2010).
[12] I. Hinder, Classical Quantum Gravity **27**, 114004 (2010).
[13] M. D. Duez, Classical Quantum Gravity **27**, 114002 (2010).
[14] E. Rantsiou, S. Kobayashi, P. Laguna, and F. A. Rasio, Astrophys. J. **680**, 1326 (2008).
[15] F. Löffler, L. Rezzolla, and M. Ansorg, Phys. Rev. D **74**, 104018 (2006).
[16] J. A. Faber, T. W. Baumgarte, S. L. Shapiro, K. Taniguchi, and F. A. Rasio, Phys. Rev. D **73**, 024012 (2006).
[17] J. A. Faber, T. W. Baumgarte, S. L. Shapiro, and K. Taniguchi, Astrophys. J. Lett. **641**, L93 (2006).
[18] M. Shibata and K. Uryu, Phys. Rev. D **74**, 121503(R) (2006).
[19] M. Shibata and K. Uryu, Classical Quantum Gravity **24**, S125 (2007).
[20] M. Shibata and K. Taniguchi, Phys. Rev. D **77**, 084015 (2008).
[21] T. Yamamoto, M. Shibata, and K. Taniguchi, Phys. Rev. D **78**, 064054 (2008).
[22] Z. B. Etienne, J. A. Faber, Y. T. Liu, and S. L. Shapiro, K. Taniguchi, and T. W. Baumgarte, Phys. Rev. D **77**, 084002 (2008).
[23] Z. B. Etienne, Y. T. Liu, S. L. Shapiro, and T. W. Baumgarte, Phys. Rev. D **79**, 044024 (2009).
[24] M. D. Duez, F. Foucart, L. E. Kidder, H. P. Pfeiffer, M. A. Scheel, and S. A. Teukolsky, Phys. Rev. D **78**, 104015 (2008).
[25] M. Shibata, K. Kyutoku, T. Yamamoto, and K. Taniguchi, Phys. Rev. D **79**, 044030 (2009).
[26] K. Kyutoku, M. Shibata, and K. Taniguchi, Phys. Rev. D **79**, 124018 (2009).
[27] P. M. Motl, M. Anderson, M. Besselman, S. Chawla, E. W. Hirschmann, L. Lehner, S. L. Liebling, D. Neilsen, and J. E. Tohline, Bull. Am. Phys. Soc. **41**, 295 (2010).
[28] S. Chawla, M. Anderson, M. Besselman, L. Lehner, S. L. Liebling, P. M. Motl, and D. Neilsen, Phys. Rev. Lett. **105**, 111101 (2010).
[29] M. D. Duez, F. Foucart, L. E. Kidder, C. D. Ott, and S. A. Teukolsky, Classical Quantum Gravity **27**, 114106 (2010).
[30] F. Pannarale, A. Tonita, and L. Rezzolla, Astrophys. J. **727**, 95 (2011).
[31] F. Foucart, M. D. Duez, L. E. Kidder, and S. A. Teukolsky, Phys. Rev. D **83**, 024005 (2011).
[32] K. Kyutoku, M. Shibata, and K. Taniguchi, Phys. Rev. D **82**, 044049 (2010).

[33] V. Paschalidis, M. MacLeod, T. W. Baumgarte, and S. L. Shapiro, Phys. Rev. D **80**, 024006 (2009).

[34] T. W. Baumgarte, S. L. Shapiro, and M. Shibata, Astrophys. J. **528**, L29 (2000).

[35] I. A. Morrison, T. W. Baumgarte, and S. L. Shapiro, Astrophys. J. **610**, 941 (2004).

[36] G. B. Cook, S. L. Shapiro, and S. A. Teukolsky, Astrophys. J. **422**, 227 (1994).

[37] A. Akmal, V. R. Pandharipande, and D. G. Ravenhall, Phys. Rev. C **58**, 1804 (1998).

[38] C. P. Lorenz, D. G. Ravenhall, and C. J. Pethick, Phys. Rev. Lett. **70**, 379 (1993).

[39] R. B. Wiringa, V. Fiks, and A. Fabrocini, Phys. Rev. C **38**, 1010 (1988).

[40] V. R. Pandharipande and R. A. Smith, Bull. Am. Phys. Soc. **7**, 240 (1975) .

[41] H. A. Bethe and M. B. Johnson, Nucl. Phys. **A230**, 1 (1974).

[42] V. R. Pandharipande, Nucl. Phys. **A174**, 641 (1971).

[43] G. Nelemans, L. R. Yungelson, and S. F. P. Zwart, Astron. Astrophys. **375**, 890 (2001).

[44] A. Cooray, Mon. Not. R. Astron. Soc. **354**, 25 (2004).

[45] T. A. Thompson, M. D. Kistler, and K. Z. Stanek, arXiv:0912.0009.

[46] S. Rappaport, P. C. Joss, and R. F. Webbink, Astrophys. J. **254**, 616 (1982).

[47] S. Rappaport, F. Verbunt, and P. C. Joss, Astrophys. J. **275**, 713 (1983).

[48] F. Verbunt and S. Rappaport, Astrophys. J. **332**, 193 (1988).

[49] P. Podsiadlowski, P. C. Joss, and J. J. L. Hsu, Astrophys. J. **391**, 246 (1992).

[50] T. R. Marsh, G. Nelemans, and D. Steeghs, Mon. Not. R. Astron. Soc. **350**, 113 (2004).

[51] W. Benz, R. Bowers, A. Cameron, and W. Press, Astrophys. J. **348**, 647 (1990).

[52] F. A. Rasio and S. L. Shapiro, Astrophys. J. **438**, 887 (1995).

[53] L. Segretain, G. Chabrier, and R. Mochkovitch, Astrophys. J. **481**, 355 (1997).

[54] J. Guerrero, E. Garcia-Berro, and J. Isern, Astron. Astrophys. **413**, 257 (2004).

[55] S.-C. Yoon, P. Podsiadlowski, and S. Rosswog, Mon. Not. R. Astron. Soc. **380**, 933 (2007).

[56] M. Dan, S. Rosswog, and M. Brüggen, J. Phys. Conf. Ser. **172**, 012034 (2009).

[57] K. Thorne and A. Zytkow, Astrophys. J. **212**, 832 (1977).

[58] Z. Etienne, Y. T. Liu, and S. L. Shapiro, Phys. Rev. D **82**, 084031 (2010).

[59] S. L. Shapiro and S. A. Teukolsky, *Black Holes, White Dwarfs, and Neutron Stars* (John Wiley & Sons, New York, 1983).

[60] J. S. Read, B. D. Lackey, B. J. Owen, and J. L. Friedman, Phys. Rev. D **79**, 124032 (2009).

[61] R. Arnowitt, S. Deser, and C. Misner, *Gravitation: An Introduction to Current Research* (Cambridge University Press, Wiley, New York, 1962).

[62] T. W. Baumgarte and S. L. Shapiro, Phys. Rep. **376**, 41 (2003).

[63] T. W. Baumgarte, G. B. Cook, M. A. Scheel, S. L. Shapiro, and S. A. Teukolsky, Phys. Rev. D **57**, 7299 (1998).

[64] S. Balay, K. Buschelman, W. D. Gropp, D. Kaushik, M. G. Knepley, L. C. McInnes, B. F. Smith, and H. Zhang, PETSc Web page (2009), http://www.mcs.anl.gov/petsc.

[65] S. Balay, K. Buschelman, V. Eijkhout, W. D. Gropp, D. Kaushik, M. G. Knepley, L. C. McInnes, B. F. Smith, and H. Zhang, Argonne National Laboratory Tech. Report No. ANL-95/11 Revision 3.0.0, 2008.

[66] S. Balay, W. D. Gropp, L. C. McInnes, and B. F. Smith, in *Modern Software Tools in Scientific Computing*, edited by E. Arge, A. M. Bruaset, and H. P. Langtangen (Birkhäuser Press, Boston, 1997), p. 163.

[67] M. D. Duez, Y. T. Liu, S. L. Shapiro, and B. C. Stephens, Phys. Rev. D **72**, 024028 (2005).

[68] M. Shibata and T. Nakamura, Phys. Rev. D **52**, 5428 (1995).

[69] T. W. Baumgarte and S. L. Shapiro, Phys. Rev. D **59**, 024007 (1998).

[70] J. R. van Meter, J. G. Baker, M. Koppitz, and D.-I. Choi, Phys. Rev. D **73**, 124011 (2006).

[71] http://www.cactuscode.org/.

[72] E. Schnetter, S. H. Hawley, and I. Hawke, Classical Quantum Gravity **21**, 1465 (2004).

[73] P. Colella and P. R. Woodward, J. Comput. Phys. **54**, 174 (1984).

[74] A. Harten, and P. D. Lax, and B. van Leer SIAM Rev. **25**, 35 (1983).

[75] Z. Etienne, Y. T. Liu, S. Shapiro, and T. Baumgarte, Phys. Rev. D **79**, 044024 (2009).

[76] R. J. Leveque, *Finite Volume Methods for Hyperbolic Problems* (Cambridge University Press, Cambridge, England, 2002).

[77] V. Alexander, Ph.D. thesis, RWTH Aachen, 2005, online at http://darwin.bth.rwth-aachen.de/opus/volltexte/2005/1210/.

[78] J. W. Murphy, C. D. Ott, and A. Burrows, Astrophys. J. **707**, 1173 (2009).

[79] M. Saijo and I. Hawke, Phys. Rev. D **80**, 064001 (2009).